Publications of the Astronomical Society of Australia (2019), **36**, e035, 25 pages
doi:10.1017/pasa.2019.23

CAMBRIDGE UNIVERSITY PRESS

Research Paper

R_e. I. Understanding galaxy sizes, associated luminosity densities, and the artificial division of the early-type galaxy population

Alister W. Graham

Centre for Astrophysics and Supercomputing, Swinburne University of Technology, Hawthorn, Victoria 3122, Australia

Abstract

For decades, the deceptive simplicity of the radius R_e, enclosing an arbitrary 50% of a galaxy's light, has hamstrung the understanding of early-type galaxies (ETGs). Half a century ago, using these 'effective half-light' radii from de Vaucouleurs' $R^{1/4}$ model, Sérsic reported that bright ETGs follow the relation $\mathfrak{M}_B \propto 2.5 \log R_e$; and consequently, one has that $\langle\mu\rangle_e \propto 2.5 \log R_e$ and $\mu_e \propto 2.5 \log R_e$, where μ_e and $\langle\mu\rangle_e$ are the effective surface brightness at R_e and the mean effective surface brightness within R_e, respectively. Sérsic additionally observed an apparent transition which led him to advocate for a division between what he called dwarf and giant ETGs; a belief frequently restated to occur at $\mathfrak{M}_B \approx -18$ mag or $n \approx 2.5$. Here, the location of this false dichotomy in diagrams using 'effective' parameters is shown to change by more than 3 mag simply depending on the arbitrary percentage of light used to quantify a galaxy's size. A range of alternative radii are explored, including where the projected intensity has dropped by a fixed percentage plus a battery of internal radii, further revealing that the transition at $\mathfrak{M}_B \approx -18$ mag is artificial and does not demark a boundary between different physical processes operating on the ETG population.

The above understanding surrounding the effective radius R_e is of further importance because quantities such as dynamical mass $\sigma^2 R/G$, gravitational-binding energy GM^2/R, acceleration GM/R^2, and the 'Fundamental Plane' also depend on the arbitrary percentage of light used to define R, with implications for dark matter estimates, galaxy formation theories, compact massive galaxies, studies of peculiar velocity flows, and more. Finally, some of the vast literature which has advocated for segregating the ETG population at $\mathfrak{M}_B \approx -18$ mag ($M \approx 1$–2×10^{10} $M_\odot$) is addressed, and it is revealed how this pervasive mindset has spilled over to influence both the classical bulge versus pseudobulge debate and recently also correlations involving supermassive black hole masses.

Keywords: galaxies: bulges — galaxies: dwarf — galaxies: elliptical and lenticular, cD — galaxies: formation — galaxies: fundamental parameters — galaxies: structure.

(Received 09 February 2019; revised 07 May 2019; accepted 09 May 2019)

1. Introduction

During the first half of the 20th century, astronomers developed several empirical functions to describe the observed, that is, projected on the plane of the sky, radial distribution of light in external galaxies. These functions provided physical measurements which enabled astronomers to better answer simple questions such as, How big is it, and, How bright is it? This helped to place extragalactic astronomy on a more scientific footing, elevating some sky surveys above the somewhat derogatory status of 'stamp collecting'.

For both early-type galaxies (ETGs) and late-type galaxies (LTGs), these mathematical functions had two parameters: one stretched the model light profile along the horizontal (radial) axis and the other stretched it along the vertical (intensity) axis. One could arbitrarily set the scale radius to be where the intensity had dropped by some fixed factor from the central intensity, or it could be set as the radius effectively enclosing some fixed fraction of the total light, such as 50% or 90%. Due to the homologous nature of these two-parameter models, defining the scale radius or the scale intensity in a different way would shift all galaxies equally in diagrams involving the logarithm of these model-determined quantities. As such, trends and patterns in such diagrams were not dependent on how these scale parameters were set. However, if galaxies are not adequately described by these two-parameter functions, then the galaxies' distribution in the scaling diagrams can become a function of the arbitrarily defined scale radius and scale intensity.

The above fact, and the implications of the above fact, has not been adequately realised in the literature, and countless papers have drawn questionable scientific conclusions based upon the distribution of galaxies in diagrams involving a galaxies' arbitrary 50% radius and the intensity associated with this radius. Given that this has gone on for decades, this paper goes to some length to try and carefully explain the curved distribution of ETGs in diagrams involving effective half-light parameters. These curved distributions have been used many times in the literature to argue for a distinct divide among the ETG population into dwarf and giant[a] ETGs separated at the bend midpoint: $\mathfrak{M}_B \approx -18$ mag (e.g.

Author for correspondence: Alister W. Graham, Email: AGraham@swin.edu.au

Cite this article: Graham AW. (2019) R_e. I. Understanding galaxy sizes, associated luminosity densities, and the artificial division of the early-type galaxy population. *Publications of the Astronomical Society of Australia.* **36**, e035, 1–25. https://doi.org/10.1017/pasa.2019.23

[a]In the literature, 'giant' ETGs are also referred to as 'ordinary' or 'normal' ETGs, or often simply as 'elliptical' (E) galaxies, as distinct from the 'dwarf elliptical' (dE) galaxies

Kormendy et al., 2009, hereafter K09; Kormendy & Bender, 2012; Kormendy, 2016; Tolstoy, Hill, & Tosi, 2009; Somerville & Davé, 2015). In order to help better appreciate this issue and more fully understand galaxy structure, the curved distributions of ETGs in diagrams involving radii that enclose different percentages of the total light are presented, and it is revealed how the absolute magnitude associated with the midpoint of the bend changes considerably.

Advocates for an ETG dichotomy have alleged that the formation physics must be dramatically different for ETGs fainter and brighter than $\mathfrak{M}_B \approx -18$ mag, because the slope of certain scaling relations is different at magnitudes fainter and brighter than this. For example, Kormendy & Djorgovski (1989; see their Section 8) wrote, 'A fundamental application of parameter correlations has been the demonstration that diffuse dwarf spheroidal[b] galaxies are a family of objects unrelated to ellipticals'. This claim was, however, at odds with other research that did not use effective half-light parameters and instead advocated for a continuity among the ETG population at $\mathfrak{M}_B \approx -18$ mag (e.g. Caldwell, 1983*a*, see his Figure 6; Binggeli, Sandage, Tarenghi, 1984; Sandage et al. 1985; Binggeli, Sandage, & Tammann 1985; Bothun et al., 1986, see their Figure 7; Caldwell & Bothun, 1987).

As noted by James (1994), the shape of ETG light profiles had also been considered one of the principal differences separating dwarf and ordinary ETGs — with 'dwarf' ETGs having exponential light profiles (similar to the discs of LTGs) and 'ordinary' ETGs having $R^{1/4}$ profiles — emboldening those interpreting transitions in certain scaling diagrams as evidence of different formation physics at magnitudes fainter and brighter than $\mathfrak{M}_B \approx -18$ mag. However, as we shall see, the systematically changing (with absolute magnitude) shape of the ETG light profile, that is, structural non-homology, is key to understanding the unification of dwarf and ordinary ETGs.

To understand the mechanics of the structural parameter scaling diagrams, Section 2 of this paper provides a context-setting background using de Vaucouleurs' $R^{1/4}$ model and Sérsic's $R^{1/n}$ model, and provides a familiarity with the model parameters R_e and both the surface brightness at R_e, denoted by μ_e, and the average surface brightness within R_e, denoted by $\langle\mu\rangle_e$. Section 3 then presents two key empirical relations, providing the foundation for the insight which follows.

Equipped with the above background knowledge, Section 4 presents an array of scaling relations based on radii and surface brightnesses which effectively enclose different fixed percentages of the galaxy light. It soon becomes apparent why the μ_e–R_e relation is itself quite tight for bright ETGs but not for faint ETGs. 4.2 then goes on to explore a range of alternative radii and surface brightnesses. In particular, radii where the intensity has dropped by a fixed percentage are introduced, and the use of isophotal radii is revisited in 4.3. Section 5 expands on the analysis using internal radii that define spheres that effectively enclose a fixed percentage of the galaxy light. These internal radii include 'effective' radii plus the new radii where the internal density has declined by a fixed amount, isodensity radii, virial radii, and new Petrosian-like radii. The changing location of the bend midpoint in various scaling relations reveals that it has nothing to do with changing physical processes but is instead merely a result of the arbitrary definition used to quantify the sizes of ETGs.

Section 6 presents ETG data from Ferrarese et al. (2006) and K09, and resolves the different interpretations given in those papers. Finally, a discussion in Section 7 broaches some of the literature which has advocated for a dichotomy of the ETG population at $\mathfrak{M}_B \approx -18$ mag. Considerable historical context is included to aid the reader in understanding how the topic evolved. This is also partly necessary because support for interpreting these curved relations, in terms of different formation processes at magnitudes brighter and fainter than the bend midpoint at $\mathfrak{M}_B \approx -18$ mag, attracted a range of bright ideas over the years and many of these are sometimes heralded without adequate qualification. Some of the literature surrounding the similar separation of bulges into 'classical' or 'pseudobulge' is also discussed. Bulge scaling relations, as distinct from ETG scaling relations, are also discussed in the context of high-z compact massive systems, which by all accounts appear to be the bulges of massive local galaxies. In addition, Subsection 7.5 reveals why the 'Fundamental Plane', involving the velocity dispersion σ (Djorgovski and Davis, 1987; see also Fish, 1963), is tighter than the μ_e–R_e relation for ordinary ETGs, and a warning about fitting and interpreting 2D planes to curved distributions involving supermassive black hole mass and 'effective' parameters is also issued.

2. Mathematical background

2.1. de Vaucouleurs' $R^{1/4}$ model

First in French (de Vaucouleurs, 1948) then in English, de Vaucouleurs (1953) presented an empirical function that was to become known as the $R^{1/4}$ model due to how the projected (on the plane of the sky) intensity profile $I(R)$ depends on the projected radius R raised to the 1/4 power. This mathematical model can be expressed as

$$I(R) = I_0 \exp\left[-b\left(\frac{R}{R_s}\right)^{1/4}\right] = \frac{I_0}{\left(e^b\right)^{(R/R_s)^{1/4}}}, \quad (1)$$

where R_s is a scale radius, I_0 is a scale intensity at $R = 0$, and b is a constant that shall be explained below. Given that the galaxies do not have clear edges — and in the middle of the 20th century it was not known how their radial profiles behaved at large radii — the practice was to extrapolate one's adopted model to infinity in order to determine a galaxy's total luminosity.

The projected luminosity (from three dimensions to two dimensions onto the plane of the sky) interior to a circle of radius R is determined by integrating the intensity over the enclosed area, such that

$$L(<R) = \int_0^R I(R')2\pi R' \mathrm{d}R'. \quad (2)$$

Using the substitution $x = b(R/R_s)^{1/4}$ in equation (1), the above integral reduces to

$$L(<R) = \frac{I_0 R_s^2 8\pi}{b^8}\gamma(8,x), \quad (3)$$

where γ(8,x) is the incomplete gamma function defined by

$$\gamma(8,x) = \int_0^x e^{-t} t^{8-1} \mathrm{d}t. \quad (4)$$

As noted, the total luminosity is obtained by integrating to infinity, in which case $\gamma(8,x)$ is replaced with the complete gamma function, $\Gamma(8)$, and one has that

fainter than $\mathfrak{M}_B = -18$ mag (Sandage & Binggeli, 1984, using $H_0 = 50$ km s^{-1} Mpc^{-1}) or two-thirds of a magnitude fainter using $H_0 = 67.8$ km s^{-1} Mpc^{-1} (Planck et al., 2016).

[b]Kormendy & Djorgovski (1989) consider 'dwarf spheroidal' galaxies to appear at $\mathfrak{M}_B \gtrsim -18$ mag rather than the more commonly used values of $\approx -13\pm$ mag. In order to better emphasise their view of a distinct population from the 'ordinary elliptical' galaxies brighter than $\mathfrak{M}_B \approx -18$ mag, they use this term to describe what others call 'dwarf elliptical' galaxies ($-13 \gtrsim \mathfrak{M}_B \gtrsim -18$ mag).

https://doi.org/10.1017/pasa.2019.23 Published online by Cambridge University Press

$$L_{\rm tot} = \frac{I_0 R_{\rm s}^2 8\pi}{b^8}\Gamma(8). \quad (5)$$

Now, here is where things can, and did, become arbitrary. Gerard de Vaucouleurs elected to define the radius $R_{\rm s}$ such that it enclosed 50% of the total light $L_{\rm tot}$. He did this by determining the value of b required to balance the equation

$$\gamma(8, b) = 0.5\,\Gamma(8). \quad (6)$$

With $b = -7.669$, the projected radius $R_{\rm s}$ effectively encloses half of the model's total light, and it was subsequently denoted $R_{\rm e}$ and referred to as the 'effective half light radius'. The $R^{1/4}$ model's central surface brightness, μ_0, is given by $-2.5\log I_0$, and the projected intensity at $R = R_s \equiv R_{\rm e}$ is given by

$$I_{\rm e} = I_0 {\rm e}^{-b} = I_0/2141. \quad (7)$$

The average intensity $\langle I\rangle_{\rm e}$ within $R_{\rm e}$ is such that

$$0.5\,L_{\rm tot} = \pi R_{\rm e}^2 \langle I\rangle_{\rm e}, \quad (8)$$

and it can be shown that

$$\langle I\rangle_{\rm e} = 3.61 I_{\rm e} = I_0/594 \quad (9)$$

(Graham & Driver, 2005, see their equations 7 and 9).

As alluded to above, de Vaucouleurs *could* have chosen a radius enclosing any fraction of the light, and his two-parameter model would still have the same functional form (equation (1)). That is, one could use a radius R_X containing any percentage of the total light, and one could use an intensity I_Y taken from any (similar or different) fixed radius (in units of $R_{\rm e}$). The homology of the $R^{1/4}$ model is such that $R_X = C_1 R_{\rm e}$, $I_Y = C_2 I_{\rm e}$, and $\langle I\rangle_Y = C_3\langle I\rangle_{\rm e}$, where C_1, C_2, and C_3 are constants. In trying to understand the behaviour of, and connections between, galaxies, astronomers could plot $\log R_X$ versus $-2.5\log I_Y$, and versus $-2.5\log\langle I\rangle_Y$, and the trends would be the same as obtained when using $R_{\rm e}$, $I_{\rm e}$, and $\langle I\rangle_{\rm e}$, just shifted vertically or horizontally in one's diagram. As such, the arbitrary selection of 50% by de Vaucouleurs did not appear to matter. To give a more concrete example, de Vaucouleurs could have set the scale radius $R_s = R_{10}$, that is, enclosing 10% of the total light (e.g. Farouki, Shapiro, & Duncan, 1983). The mean intensity $\langle I\rangle_{10}$ within this radius is related by the expression

$$0.1\,L_{\rm tot} = \pi R_{10}^2 \langle I\rangle_{10}, \quad (10)$$

and the associated value of b is obtained by solving the equation

$$\gamma(8, b) = \Gamma(8)/10, \quad (11)$$

to give $b = 4.656$ and $I_{10} = I_0 {\rm e}^{-b} = I_0/105.2$ (cf. equation (7)). In this example, de Vaucouleurs' model would then read

$$I(R) = I_0 \exp\left[\frac{-4.656}{R_{10}^{1/4}} R^{1/4}\right], \quad (12)$$

where $R_{10} = (4.656/7.669)^4\,R_{\rm e} = R_{\rm e}/7.361$, and $\langle I\rangle_{10} = I_0/54.77$.

However, and this is the crux of the matter: ETGs, and also the bulges of spiral galaxies, do not follow the $R^{1/4}$ model, that is, there is not structural homology. This has important consequences when using radii enclosing a fixed percentage of the total light, and when using the associated surface brightness terms.

It is noted that the $R^{1/4}$ model had become so entrenched during the second half of the 20th century that it was invariably referred to as the $R^{1/4}$ *law*. That is, this empirical model was effectively elevated to the status of a physical law because it was thought that all ETGs did have $R^{1/4}$ light profiles. Indeed, it was not uncommon for astronomers to vary the sky-background in order to make their light profiles more $R^{1/4}$-like (e.g. Tonry et al., 1997; see also the 'Seven Samurai' team data from Burstein et al., 1987 as presented in D'Onofrio, Capaccioli, & Caon 1994, their Figure 4). This belief was in part because of de Vaucouleurs (1959) study that had shown that the $R^{1/4}$ model fit better than the popular Reynolds' (1913) model[c], and because of de Vaucouleurs & Capaccioli's (1979) study of NGC 3379 which revealed that its light profile is remarkably well fit by the $R^{1/4}$ model over an extensive range in surface brightness (see also Fish, 1964 in the case of M87 and M105). However, Caon, Capaccioli, & D'Onofrio (1993 1994 1990) and D'Onofrio et al. (1994), subsequently revealed that other ETGs, with different absolute magnitudes, are equally well fit down to B-band surface brightnesses of $\sim$28 mag arcsec^{-2} when using exponents in the light profile model that are different to the value of 1/4.

2.2. Sérsic's $R^{1/n}$ model

Today, it is widely recognised[d] that ETGs — and the bulges of spiral galaxies — display a range of light profile shapes that are better represented by a generalised version of the $R^{1/4}$ model, referred to as the Sérsic (1963) $R^{1/n}$ model, in which the exponent $1/n$ can take on a range of values other than just 1/4. This realisation applies to not just the ordinary ETGs (e.g. Caon et al., 1993; D'Onofrio et al., 1994) but also the dwarf ETGs (e.g. Davies et al., 1988; Cellone, Forte & Geisler, 1994; James, 1994; Vennik & Richter, 1994; Young & Currie, 1994, 1995) which had previously been fit with an exponential model (e.g. Faber & Lin, 1983; Binggeli et al., 1984). Despite this, the early assumption of structural homology for dwarf ETGs versus a different structural homology for giant ETGs had been sown into the astronomical literature and psyche. Moreover, the implications of a varying exponent upon the use of the arbitrary 50% half-light radius, and the associated surface brightness terms, remained poorly recognised.

José Sérsic's (1963, 1968a) $R^{1/n}$ model, which was introduced in Spanish, is a generalisation of de Vaucouleurs' $R^{1/4}$ model such that

$$\begin{aligned} I(R) &= I_0 \exp\left[-b_n\left(\frac{R}{R_{\rm e}}\right)^{1/n}\right] = \frac{I_0}{\left({\rm e}^{b_n}\right)^{(R/R_{\rm e})^{1/n}}} \\ &= I_{\rm e} \exp\left\{-b_n\left[\left(\frac{R}{R_{\rm e}}\right)^{1/n} - 1\right]\right\}. \end{aligned} \quad (13)$$

The exponent $1/n$, or its inverse n, describes the curvature of the light profile. Within $\approx 1R_{\rm e}$, a larger value of n results in a more centrally concentrated distribution of light, while beyond $\approx 1R_{\rm e}$, a larger value of n results in a less steeply declining light profile. The quantity b_n was defined such that $I_{\rm e}$ is, again, the intensity at the 'effective half light' radius $R_{\rm e}$ that encloses half of the total light (Capaccioli, 1989; Ciotti, 1991; Caon et al., 1993). The value of b_n is solved via the equation

$$\gamma(2n, b_n) = 0.5\,\Gamma(2n) \quad (14)$$

(cf. equation (6)), and the total luminosity, giving the total magnitude, is given by

$$L_{\rm tot} = \frac{I_0 R_{\rm e}^2 2n\pi}{(b_n)^{2n}}\Gamma(2n) \quad (15)$$

(cf. equation (5)). For $0.5 < n < 10$, $b_n \approx 1.9992n - 0.3271$ (Capaccioli, 1989).

[c]The Reynolds' (1913) model was, somewhat unfairly, later referred to as Hubble's (1930) model.

[d]See the reviews by Graham (2013, 2016) and references therein.

https://doi.org/10.1017/pasa.2019.23 Published online by Cambridge University Press

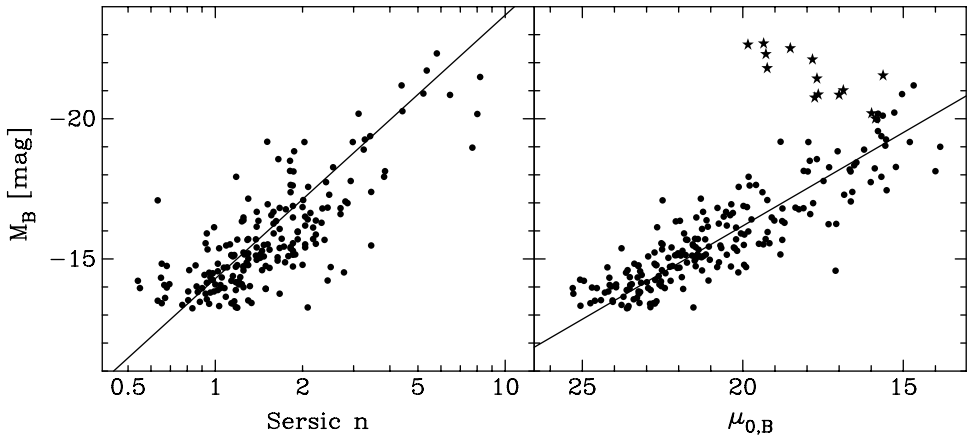

Figure 1. Left panel: Absolute *B*-band magnitude (Vega) versus the logarithm of the *B*-band Sérsic index *n* for ETGs. Right panel: Absolute magnitude versus the *B*-band central surface brightness $\mu_{0,B}$. Figure adapted from Graham (2013), with data from Binggeli & Jerjen (1998), Stiavelli et al. (2001), Graham & Guzmán (2003), Caon et al. (1993), D'Onofrio et al. (1994), and Faber et al. (1997, with stars representing their 'core-Sérsic' galaxies). The core-Sérsic galaxies have partially depleted cores with fainter central surface brightnesses than the relation shown (Equation (17)). However, the inward extrapolation of these galaxies' outer Sérsic profile yields $\mu_{0,B}$ values which follow the relation, as noted by Jerjen and Binggeli (1997).

However, what was initially (for the $R^{1/4}$ model) an inconsequential selection of an arbitrary scale radius enclosing 50% of the light now has considerable consequences given that galaxies do not all have the same light profile shape, that is, the same value of *n*. Crucially, the ratio between radii containing different fixed percentages of the projected galaxy light is no longer a constant value — as we just saw it was for the $R^{1/4}$ model — but rather changes with the Sérsic index *n*. Given that ETGs and bulges possess a range of light profile shapes that are described well by the $R^{1/n}$ model (e.g. Caon et al., 1993; D'Onofrio et al., 1994), this remark about the changing ratio of radii holds even if one does not fit an $R^{1/n}$ model but instead measures the radii independently of any light profile model.

What this means is that the distribution of points in scaling diagrams involving the logarithm of scale radii and scale intensities will look different depending on what scale radius is used. That is, the arbitrary choice of radius, which to date has been the 50% radius, produces a somewhat arbitrary pattern in diagrams using $\log R_{\rm e}$, $\mu_{\rm e,}$ and $\langle\mu\rangle_{\rm e}$. Also apparent, from equation (13), is that the scale radius no longer occurs where the intensity has declined by the same fixed amount but rather by different amounts depending on the value of e^{b_n} and thus on the value of *n*. To quantify this, 4.1 will explore scaling diagrams using projected radii containing fixed percentages of the total light, including 50%, revealing how the bend in scaling relations using 'effective' parameters changes. 4.2 will explore the use of scale radii where the intensity has dropped by the same amount, yielding monotonic size–luminosity relations without the strong bends seen in 4.1.

3. Two key empirical relations: $\mathfrak{M}$–log *n* and $\mathfrak{M}$–μ_0

Two key linear scaling relations describe the structural properties of ETGs. These have been known for decades and were common in the 1960s, 1970s, and early 1980s before somewhat falling from favour as the 'effective' parameters from the $R^{1/4}$ model started to dominate the landscape.

The first relation relates to the central concentration of the galaxy light.[e] This was the primary criteria of the concentration classes in the Yerkes system (e.g. Morgan, 1958, 1959, 1962) although introduced to match the changing spectra along the Aitken–Jeans–Lundmark–Hubble[f] sequence (Graham 2019) as observed by Morgan & Mayall (1957). Fraser (1972) subsequently quantified the concentration using C_{21}, the ratio of radii containing 50 and 25% of the total light, and C_{32}, the ratio of radii containing 75 and 50% of the total light[g]. Subsequently, de Vaucouleurs (1977) extended this to the use of C_{31} (e.g. Kent, 1985). The linear concentration–magnitude relation for dwarf and ordinary ETGs has been known since at least Binggeli et al. (1984, see their Figure 10) and Ichikawa, Wakamatsu, & Okamura (1986, see their Figure 11). Using the *B*-band absolute magnitude $\mathfrak{M}_B$, the left panel of Figure 1 shows the $\mathfrak{M}_B$–log *n* (hereafter $\mathfrak{M}_B$–*n* for brevity) diagram, taken from Graham & Guzmán (2003, see their Figure 10). The Sérsic index is a measure of the radial concentration of galaxy light (King, 1966, see the end of his Section IV; Trujillo, Graham, & Caon 2001, see their Section 3). Other examples of the $\mathfrak{M}_B$–*n* diagram can be seen in Caon et al. (1993), James (1994), Young & Currie (1994, 1995), Graham et al. (1996), Jerjen, Binggeli, & Freeman (2000, see their Figure 6), Ferrarese et al. (2006), and K09.

The right panel of Figure 1 reproduces the $\mathfrak{M}_B$–(central surface brightness, $\mu_{0,B}$) diagram from Graham & Guzmán (2003, see their Figure 9). The two relations in Figure 1 are such that

$$\mathfrak{M}_B = -9.4\log(n) - 14.3, \text{ and} \quad (16)$$

$$\mathfrak{M}_B = (2/3)\mu_{0,B} - 29.5. \quad (17)$$

All parameters are measured in the *B*-band on the Vega magnitude system. To avoid confusion, no subscript *B* is assigned to the Sérsic index *n* — nor will such a subscript be assigned to any scale radii in this paper — although these parameters *are* slightly dependent on the filter used (e.g. Kelvin et al., 2012; Häußler et al., 2013; Kennedy et al., 2016*a*,b).

There is no bend at $\mathfrak{M}_B \approx -18$ mag in either of the above two relations (equations 16 and 17), with the exception that luminous ($\mathfrak{M}_B \lesssim -20.5$ mag) galaxies, with cores that are depleted of stars, have central surface brightnesses that deviate from the $\mathfrak{M}_B$–μ_0 relation. Such galaxies were discussed half a century ago by King & Minkowski (1966, 1972) and King (1978), and were known to

[e]Of note, Lundmark (1925), and references therein, was using the concentration to classify galaxies 100 years ago.

[f]Aitken (1906), Jeans (1919, 1928), Lundmark (1925), Hubble (1926, 1936).

[g]This followed in the footsteps of the concentration ratio introduced by King (1962, see his equation 17) for globular clusters.

https://doi.org/10.1017/pasa.2019.23 Published online by Cambridge University Press

produce a departure from the otherwise linear $\mathfrak{M}_B$–μ_0 relation (e.g. Gudehus, 1973, see his Figure 6; see Oemler, 1973 for further discussion). The cores of these 'core-Sérsic' galaxies are nowadays thought to be depleted by the coalescence of massive black holes (Begelman, Blandford, & Rees, 1980; Thomas et al., 2014), which kick (up to a few percent of) the galaxy's inner stars to higher orbits, even ejecting some as hypervelocity stars from the galaxy (Hills, 1988). Binggeli et al. (1984, see their Figure 11; see also Binggeli, & Cameron, 1991, their Figures 9 and 18) showed that if they used the central surface brightness coming from the inward extrapolation of King models, fit outside of the depleted core region, then they recovered a near linear $\mathfrak{M}_B$–μ_0 relation. Jerjen and Binggeli (1997) and Jerjen, Binggeli, & Freeman (2000, see their Figure 5) subsequently noted that bright elliptical galaxies with depleted cores follow a linear $\mathfrak{M}_B$–μ_0 relation if one uses the central surface brightness of the best-fitting Sérsic model fit outside of the core region. The continuity between the 'dwarf' and 'ordinary' ETGs that Binggeli had repeatedly demonstrated supported a single population of ETGs, from faint to bright, until the modification of galaxy cores at $\mathfrak{M}_B \approx -20.5$ mag (see also Graham & Guzmán, 2003 and Ferrarese et al., 2006, their Figure 116).

There are many computer simulations attempting to mimic, and thereby provide insight into, the evolution of real galaxies in the Universe, such as the *Illustris* simulation (e.g. Genel et al., 2014; Vogelsberger et al., 2014; Mutlu-Pakdil et al., 2018), IllustrisTNG (Weinberger et al., 2018; Wang 2019), the EAGLE simulation (Schaye et al., 2015; Trayford & Schaye, 2018), the Magneticum simulation (Remus et al., 2015; Schulze et al., 2018), plus others (e.g. Ragone-Figueroa et al., 2013; Barai et al., 2014; Gabor & Bournaud, 2014; Taylor & Kobayashi, 2014; Steinborn et al., 2015; Anglés-Alcázar et al., 2017; Taylor, Federrath, & Kobayashi, 2017). In order to check if they are realistic, they must be able to reproduce the $\mathfrak{M}_B$–n and $\mathfrak{M}_B$–μ_0 relations for ETGs. As we will see, these two relations additionally define the $\mathfrak{M}_B$–R_e luminosity–size relation (which is used to calibrate some of the simulations, such as the EAGLE project) plus the $\mathfrak{M}_B$–μ_e relation and the R_e–μ_e relation. It is recognised that constraints on the spatial resolution of simulations may inhibit the direct observation of μ_0, but it should be recoverable by fitting $R^{1/n}$ models to their light distributions.

3.1. A representative set of ETG light profiles

Given the Sérsic function and luminosity (equations 13 and 15), and armed with the two empirical equations 16 and 17, one can readily determine not only the typical Sérsic index and central surface brightness for a given (B-band) absolute magnitude but also the typical effective surface brightness at R_e, the mean effective surface brightness within R_e, and the effective half-light radius in kpc. This information has been used here to construct a representative set of surface brightness profiles for ETGs having five different absolute magnitudes, or rather, five different Sérsic indices (Figure 2, upper panel). The associated set of mean surface brightness profiles, which display the average surface brightness enclosed within the radius R, are also shown in the lower panel of Figure 2.

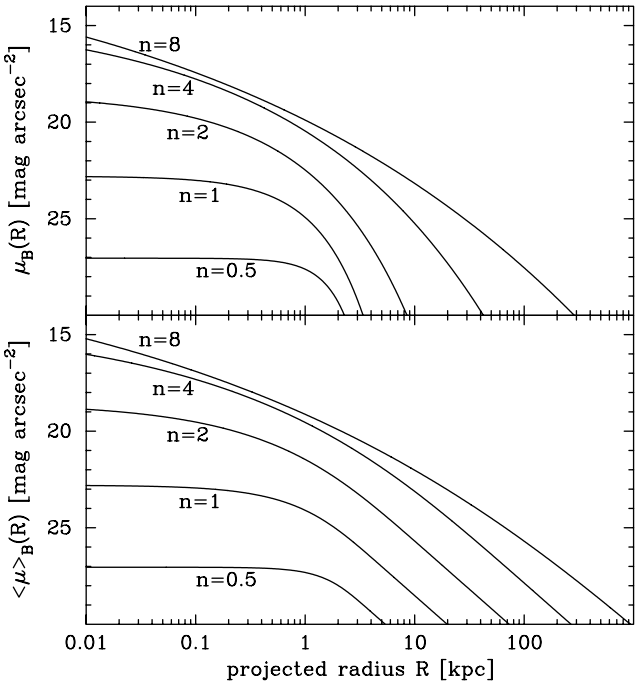

Figure 2. Upper panel: Sérsic light profiles (B-band, Vega mag), for a range of Sérsic indices n, that are representative of the ETG population at large. Lower panel: Associated set of representative mean surface brightness profiles. These stem from equations 16 and 17 and the $R^{1/n}$ model.

4. Projected parameters

4.1. Relations involving effective surface brightnesses and effective radii

This section reveals how the absolute magnitude associated with the bend in diagrams using effective radii, and effective surface brightnesses, changes depending on the percentage of light that these radii enclose. That is, it shows that the absolute magnitude associated with the bend does not relate to different formation processes but rather relates to the arbitrary definition of galaxy size.

4.1.1. Luminosity-(effective surface brightness) diagram

As was noted, given the absolute magnitude of an ETG, equations 16 and 17 inform one of the typical Sérsic index and central surface brightness μ_0 associated with this magnitude. This is enough information to determine the surface brightness μ_z, at a radius R_z, containing any fraction z (between 0 and 1, or percentage Z) of the ETG's total light. Using $\mu(R) = -2.5 \log I(R)$, at $R = R_z$, the Sérsic model (equation (13)) gives

$$\mu_z = \mu_0 + 2.5 b_{n,z} / \ln(10), \tag{18}$$

and it can be shown that the mean surface brightness is such that

$$\langle\mu\rangle_z = \mu_z - 2.5 \log[f(n)], \tag{19}$$

where

$$f(n) = \frac{z\, 2n e^{b_{n,z}}}{(b_{n,z})^{2n}} \Gamma(2n). \tag{20}$$

To date, z has invariably been set equal to 0.5, giving R_e, μ_e, and $\langle\mu\rangle_e$. The quantity $b_{n,z}$ seen above is a function of both the Sérsic index n and z, and is obtained by solving

$$\gamma(2n, b_{n,z}) = z\, \Gamma(2n) \tag{21}$$

(cf. equation (14)). Knowing $b_{n,z}$, one can additionally calculate the radius R_z containing Z percent of the total light, in terms of the effective half-light radius R_e, containing 50% of the total light:

$$R_z = \left(\frac{b_{n,z}}{b_n}\right)^n R_e, \tag{22}$$

where b_n is given by equation (14).

https://doi.org/10.1017/pasa.2019.23 Published online by Cambridge University Press

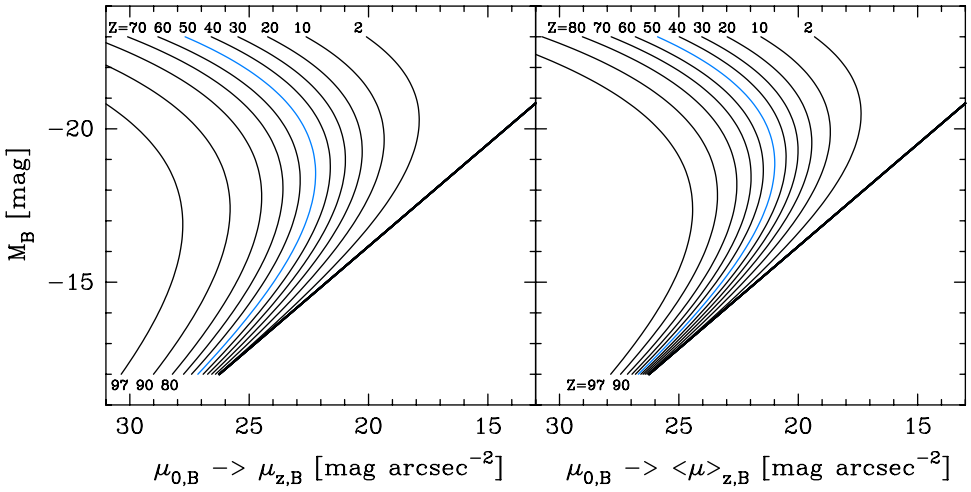

Figure 3. ETG scaling relations between absolute *B*-band magnitude and the *B*-band surface brightness at projected radii containing different percentages (Z =2, 10, 20... 80, 90, 97) of the total light (left panel) and the mean surface brightness within these radii (right panel). The thick straight line is the relation from Figure 1 involving the central surface brightness $\mu_{0,B}$. The curved lines corresponding to R_e, that is, the radius enclosing 50% ($Z = 50$, $z = 0.5$) of the total light, show the behaviour of both the effective surface brightness μ_e and the mean effective surface brightness $\langle\mu\rangle_e$. As revealed in Graham (2013, see his Figures 2–8), the ETGs in Figure 1 follow the $Z = 50$ curves shown here. The different absolute magnitude associated with the apparent midpoint or bend in the curves with different values of Z is not due to different formation physics at brighter or fainter magnitudes.

Figure 3 reveals the difference between the central surface brightness, μ_0, and both the surface brightness μ_z at the scale radius R_z (left panel) and the mean surface brightness $\langle\mu\rangle_z$ within this radius (right panel). The orthogonal behaviour (at faint and bright magnitudes) seen here for any z is a consequence of the Sérsic index changing systematically and monotonically with absolute magnitude, that is, 'structural non-homology'.

While the ETG population are unified by the linear $\mathfrak{M}$–μ_0 and $\mathfrak{M}$–log (n) relations — with no evidence for a divide at $\mathfrak{M}_B \approx -18$ mag — the peak in the bend of the ($z = 0.5$) $\mathfrak{M}$–μ_e and $\mathfrak{M}$–$\langle\mu\rangle_e$ distribution occurs at $\mathfrak{M}_B \approx -18$ mag. This has contributed to decades of belief that different physical processes have shaped the ETGs brighter and fainter than $\mathfrak{M}_B \approx -18$ mag. However, Figure 3 reveals that had de Vaucouleurs used a radius containing 97% of the total light, then some might today be claiming that the divide between dwarf and ordinary ETGs occurs at $\mathfrak{M}_B = -17$ mag; or had de Vaucouleurs used a radius containing 2% of the galaxy's total light, then they might be advocating for a divide at $\mathfrak{M}_B = -20.5$ mag.

The crucial point is that one should not assign a physical interpretation to the bend. Graham & Guzmán (2003), and Graham (2013), tried to make this point using only the $Z = 50$ curves in Figure 3 and explaining that the bend is due to the light profile shape changing smoothly as the absolute magnitude changes. That is, it is not due to different physical processes operating at absolute magnitudes fainter and brighter than −18 mag (or −17 mag or −20.5 mag).

Despite the above, there has been a remarkable number of claims of supporting evidence for the false divide at $\mathfrak{M}_B \approx -18$ mag. This often pertains to observations that some quantity (e.g. Sérsic index or colour or dynamical mass-to-light ratio) is, on average, different between ETGs brighter and fainter than $\mathfrak{M}_B \approx -18$ mag. This paper has endeavoured to more fully explain the nature of ETGs by including the additional curves in Figure 3 and by revealing in the coming sections what the distribution of ETGs looks like in related diagrams involving effective radii and other measures of radii. There is much that needs addressing given the decades of literature on this subject, the engrained nature of assigning a divide between dwarf and ordinary ETGs at $\mathfrak{M}_B = -18$ mag, and the many (yet to be widely recognised and utilised) insights from understanding these curved scaling relations.

4.1.2. Luminosity-(effective radius) diagram

Due to how the light profile smoothly and systematically changes shape with absolute magnitude (e.g. Fisher & Drory, 2010, see their Figure 13), when using effective half-light radii ($z = 0.5$), it results in a distribution of ETGs — and bulges — which is curved (e.g. Lange et al., 2015, and references therein). Here, Graham et al. (2006, see their Figure 1) and Graham & Worley (2008, see their Figure 11) are expanded upon by additionally showing what the size–luminosity relation looks like when using scale radii that effectively enclose different fractions of the total galaxy light. This also reveals how the absolute magnitude associated with the alleged dichotomy between dwarf ($\mathfrak{M}_B > -18$ mag) and ordinary ($\mathfrak{M}_B < -18$ mag) ETGs is fictitious, purely dependent on the arbitrary fraction z rather than different physical formation processes.

Building upon equation 12 from Graham & Driver (2005), which used R_e and thus $z = 0.5$, the generalised expression for the total absolute magnitude, in terms of the radius R_z containing the fraction z of the total light, is given by

$$\mathfrak{M}_{\rm tot,B} = \langle\mu\rangle_{\rm z,B} - 2.5\log(\pi R^2_{\rm z,kpc}/z) - 36.57, \qquad (23)$$

where $\langle\mu\rangle_{\rm z,B}$ is the mean surface brightness within R_z. This can be rearranged to give the expression

$$\log R_{\rm z,kpc} = \frac{\mu_0 - \mathfrak{M}_{\rm tot}}{5} + \frac{\log z - \log[f(n)]}{2} + \frac{b_{n,z}}{2\ln(10)} - 7.065, \qquad (24)$$

where $f(n)$ is given in equation (20). Using equation (17) to replace μ_0 with $\mathfrak{M}_{\rm tot}$, this expression becomes

$$\log R_{\rm z,kpc} = \frac{\mathfrak{M}_{\rm tot}}{10} + \frac{\log z - \log[f(n)]}{2} + 0.217 b_{n,z} + 1.2874. \qquad (25)$$

https://doi.org/10.1017/pasa.2019.23 Published online by Cambridge University Press

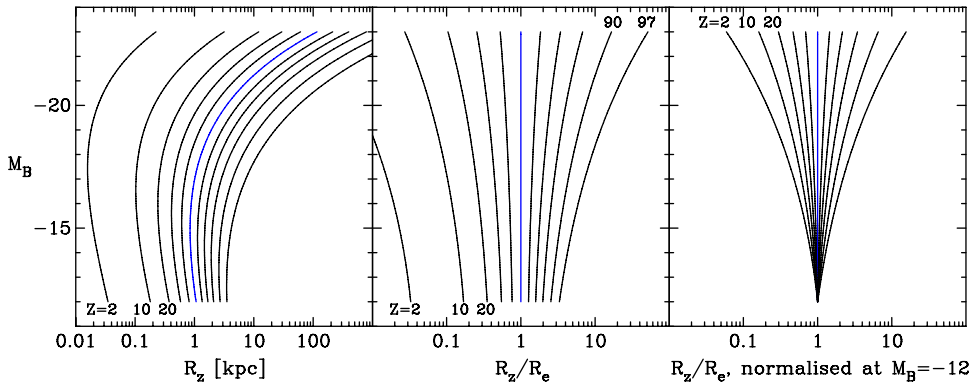

Figure 4. Left panel: relations describing the distribution of ETG *B*-band absolute magnitude versus the projected radii enclosing various percentages (Z =2, 10, 20... 80, 90, 97) of their total flux (equation (25)). The relation involving the effective half-light radius corresponds to the $Z = 50$ curve. Middle and right panels: It can be seen how much the scale radii vary depending on the arbitrary percentage of light used to define them.

The latter term in equation (25), involving z, cancels with the same term in $f(n)$, and thus the dependence of R_z on z occurs via the $b_{n,z}$ term (equation (21)).

Figure 4 presents the ETG luminosity–size relations for a range of fractions z, expressed there as a percentage Z. The curved behaviour is, once again, due to the ETG population smoothly changing its light profile shape — as quantified by the Sérsic index — with absolute magnitude. It can readily be appreciated that adopting some fixed fraction z, such as 0.5, and then claiming that different physical processes have shaped the luminosity–size relation on either side of the apparent bend-point would be a misleading endeavour (e.g. Fisher & Drory, 2010, 2016.

As can be seen in the left-hand panel of Figure 4, the bright arm of the curved $\mathfrak{M}_B$–log R_e relation for ETGs is approximately linear. This was noted by Fish (1963), who reported $\log L \propto (1 \text{ to } 1.5) \log R_e$ or equivalently $\mathfrak{M}_p \propto -(2.5 \text{ to } 3.75) \log R_e$, and can be seen in Figure 1 of Sérsic (1968b, using the data from Fish, 1964; see also Brookes and Rood, 1971; Gudehus & Hegyi, 1991; Shen et al., 2003; Graham & Worley, 2008; Lange et al., 2015)[h,i]. Sérsic (1968*b*) was perhaps the first to remark upon the offset nature of the faint ETGs from the bright ETGs in the $\mathfrak{M}_B$–log R_e diagram. Not understanding the bend in this diagram — referred to as the 'transition region' by Sérsic (1968*b*) — coupled with the inclusion of three unusually small galaxies, Sérsic attributed the bend to two populations of (dwarf and giant) elliptical galaxies, rather than one population with smoothly varying properties.

Confounding the situation further, Sérsic added LTGs into his $\mathfrak{M}_p$–log R_e diagram (see his Figure 2; cf. Figures 9 and 14 from Cappellari et al., 2013*b*). Involving R_e measures from both two-dimensional spirals and three-dimensional ellipticals, Sérsic (1968*b*) observed a slight overlap and wrote that 'it seems difficult to deny the existence of the sequence of irregulars and spirals joining that of the ellipticals in the transition region'. Kormendy (1985) adopted this same practice.

For $R_e \gtrsim$ 1–2 kpc and a photographic absolute magnitude $\mathfrak{M}_p$ brighter than −19.5 mag[j], Sérsic (1968*b*) fit a line with a slope of unity to the distribution of giant elliptical galaxies in his (log Mass)–(log R_e) diagram. This distribution resembled that in his $\mathfrak{M}$–log R_e diagram because he claims to have used a constant mass-to-light ratio of 30. As such, Sérsic (1968*b*) reported a distribution in which the absolute magnitude scaled as $-2.5 \log R_e$. Given that the magnitude of a galaxy is proportional to $\langle\mu\rangle_e - 5 \log R_e$ (e.g. de Vaucouleurs & Page, 1962, see their equation 6), one immediately has the relation $\langle\mu\rangle_e \propto 2.5 \log R_e$ for the distribution of giant elliptical galaxies. Furthermore, given that $\mu_e - \langle\mu\rangle_e = 1.393$ for the $R^{1/4}$ model that Sérsic (1968*b*) was using, one also immediately has that $\mu_e \propto 2.5 \log R_e$. This can be compared with Kormendy (1977)[k] who reported $\mu_e \propto 3.02 \log R_e$.

Somerville & Davé (2015, see their Section 1.1.4) refer to the (log Mass)–(log R_e) relation as the Kormendy relation (see also Cappellari, 2016, his Section 4.1.1), but it would be more appropriate if that title was assigned to the linear relation which Kormendy fit to the bright arm of what we now know is the curved μ_e–log R_e relation, and to instead refer to the linear (log Mass)–(log R_e) and $\mathfrak{M}$–(log R_e) relations used to describe the distribution of bright elliptical galaxies as the Fish[l] or Fish–Sérsic relation. The curved μ_e–log R_e relation is explored in 4.1.3.

Three additional insights from Figure 4 can readily be made. The first has implications for dark matter (Kent, 1990, and references therein) if using $\sigma^2 R_e$ (e.g. Poincare & Vergne, 1911; Poveda, 1958, 1961) as a proxy for mass[m] in a population of ETGs with a range of absolute magnitudes and thus a range of light profile shapes. Considering how the ratio of radii (R_{z_1}/R_{z_2}) at fixed absolute magnitude changes, for different values of z_1 and z_2 in Figure 4, one should pause for thought when using effective half-light radii ($z = 0.5$) to measure dynamical (stellar plus dark matter) masses via the proportionality $\sigma^2 R_e$ (e.g. Drory, Bender, & Hopp 2004, see their Figure 3; Cappellari et al., 2006 who use the luminosity-weighted σ values within half-light radii determined

[h]Sérsic (1968*b*) used R_e values from the $R^{1/4}$ model because he thought that the light profiles of elliptical galaxies, and the bulges of spiral galaxies, followed the $R^{1/4}$ model. His $R^{1/n}$ model (Sérsic, 1968*a*) was intended to capture varying combinations of $R^{1/4}$ bulge plus exponential disc.

[i]Excluding four erroneous references to Sérsic (1968*b*), instead of Sérsic, 1968*a* which presents the $R^{1/n}$ model, Sérsic (1968*b*) has only been cited once since 1973. Sérsic (1968*b*) and Fish (1963) are indeed over-looked papers.

[j]Based on the Hubble–Lemaître constant of 100 km s^{-1} Mpc^{-1} used by Fish, 1964, or $R_e \gtrsim$ 1.5–3.0 kpc and $\mathfrak{M}_p \approx -20.3$ mag using $H_0 = 67.8$ km s^{-1} Mpc^{-1}. This therefore matches the Sérsic/core-Sérsic divide seen in Figure 1.

[k]Kormendy (1977) additionally noted that the magnitude of each galaxy is equal to $\mu_e - 5 \log R_e - 1.9995$ based on the $R^{1/4}$ model, and thus one has $\mathfrak{M}_B \propto -1.99 \log R_e$, cf. Sérsic (1968*b*) who reported $\mathfrak{M}_B \propto -2.5 \log R_e$ for the bright ETGs.

[l]Using the $R^{1/4}$ model, Fish (1963) had previously claimed $-2.5 \log L \propto -(2.5 \text{ to } 3.75) \log R_e$ for ETGs.

[m]As derived from the virial theorem (Clausius , 1870).

https://doi.org/10.1017/pasa.2019.23 Published online by Cambridge University Press

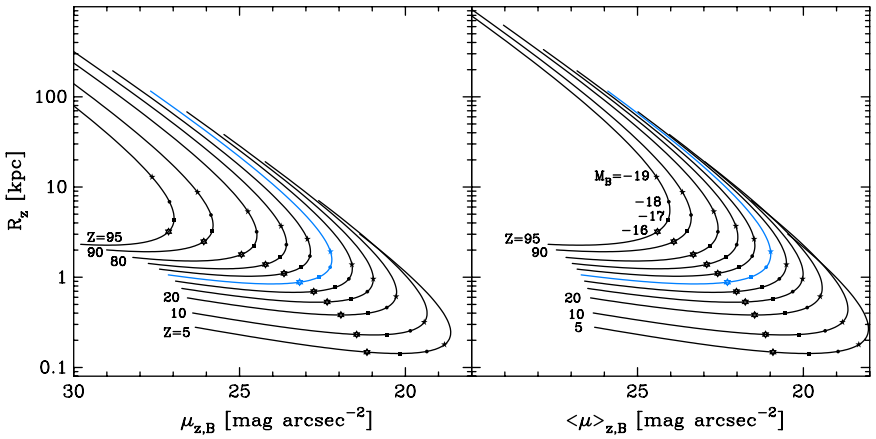

Figure 5. Size–(surface brightness) relations — describing the distribution of galaxies having a range of *B*-band absolute magnitudes (from −12 to −23 mag) — based on projected radii, R_z, enclosing different percentages (Z =5, 10, 20... 80, 90, 95) of the galaxy light. The innermost curve is associated with the 50% radius, known as the effective half-light radius R_e, the effective surface brightness μ_e at this radius (left panel), and the average surface brightness $\langle\mu\rangle_e$ within this radius (right panel). The upper envelope in the left-hand panel has a slope of ∼3.5, while the upper envelope in the right-hand panel has a slope of ∼2.8.

from $R^{1/4}$ models; Cappellari et al., 2013*a*). Using $\sigma^2 R_z$, with $z \neq 0.5$, will produce a different trend because the ratio R_e/R_z is not constant for different $\mathfrak{M}_B$ (see also the telling merger simulations by Farouki et al., 1983 revealing how R_{10}/R_e changes with mass, and the work by Campbell et al., 2017 and Lyskova et al., 2015). Therefore, it may not be appropriate to solely invoke varying fractions of dark matter to explain the systematic differences, as a function of varying absolute magnitude, between (i) this dynamical mass estimate (based on the arbitrary radius R_e) and (ii) the stellar mass estimate (obtained from the absolute magnitude). This will be broached in a subsequent study, covering the 'Fundamental Plane' (Djorgovski and Davis, 1987), improved planes, and implications for both dark matter estimates (e.g. Graves & Faber, 2010) and ETG formation (see Cappellari, 2016, his Section 4, for an overview).

Second, it is noted that the acceleration at some radius R, inside a symmetrical pressure supported system with velocity dispersion σ, is proportional to GM/R^2 or σ^2/R. Due to the structural non-homology of ETGs, this ratio will vary with M in different ways depending on what fraction z has been used to measure R. This has relevance to the critical acceleration parameter a_0, or characteristic surface density M/R^2, in modified Newtonian dynamics (Milgrom, 1983; Sanders & McGaugh, 2002, see their Figure 7; Milgrom & Sanders, 2003; Kroupa et al., 2010, their Figure 7; Misgeld & Hilker, 2011, their Figure 7; Famaey & McGaugh, 2012).

Third, it may also be insightful to explore the near-constant $R_{e,bulge}/h_{disc}$ ratio of ∼0.2 observed in spiral galaxies (e.g. Courteau et al. 1996; Graham & Worley, 2008, and references therein), which appears irrespective of whether the bulge is considered to be a 'classical' bulge or a 'pseudobulge'. For instance, the use of $z = 0.1$ or $z = 0.9$, rather than $z = 0.5$, is expected to result in this ratio systematically changing, with magnitude, by a factor of ∼3 for spiral galaxies.

4.1.3. (Effective radius)-(effective surface brightness) diagram

In addition to the R_e–μ_e and R_e–$\langle\mu\rangle_e$ distributions (derived using $z = 0.5$), it is instructive to show the size-(surface brightness) distributions R_z–μ_z and R_z–$\langle\mu\rangle_z$ that one would obtain for different values of z, corresponding to the fraction of light contained within R_z. Figure 5 reveals a number of things, three of which are worth explicitly pointing out here, while many other important but less-recognised aspects will be saved for a follow-up paper pertaining to both understanding the 'Fundamental Plane' and constructing an improved plane/surface.

First, had the community been using radii enclosing 95% or 5% of the total light, then those interpreting the bend in the corresponding size-(surface brightness) diagram may likely be claiming evidence of distinctly different formation physics for galaxies brighter and fainter than ∼ −16.5 mag or ∼ −19.5 mag, respectively.

Second, the bunching up of tracks in the top right of Figure 5 reveals why the R_e–μ_e and R_e–$\langle\mu\rangle_e$ relations have a low level of scatter for ETGs with *B*-band absolute magnitudes brighter than ≈ −19 mag. If one mis-measures the half-light radius and instead captures the radius enclosing 20, 30, 40, 60, 70, or 80% of the total light, the surface brightness terms associated with these radii are such that the galaxy's location in the R_e–μ_e diagram moves along the upper envelope seen in Figure 5 and thereby maintains a tight R_e–μ_e relation.

Third, the inclusion of ETGs fainter than $\mathfrak{M}_B \approx -19$ mag results in a thickening of the distribution in the R_e–μ_e diagram (e.g. Kodaira, Okamura, & Watanabe, 1983; Capaccioli, Caon, & D'Onofrio, 1994) as mis-measures of the half-light radius will shift galaxies perpendicular to the curved $z = 0.5$ relation at faint absolute magnitudes.

Bildfell et al. (2008) report that '*The Kormendy relation of our BCGs is steeper than that of the [less luminous] local ellipticals, suggesting differences in the assembly history of these types of systems*'. Although the literature is full of similar claims, such interpretations are not appropriate given the curved R_e–μ_e relation's dependence on the arbitrary value $z = 0.5$. Countless studies which have attached a physical significance to slopes and bends in scaling diagrams involving the logarithm of R_e, μ_e, and/or $\langle\mu\rangle_e$ should be questioned. As already noted in Graham & Guzman (2004) and Graham (2005), this remark extends to studies of the 'Fundamental Plane' (Guzmán et al. 2019, in preparation).

A range of other measures for galaxy size is explored in the remainder of this section.

4.2. An alternative scheme for defining projected radii

The previous text focused on projected radii that enclosed an arbitrary fraction of light relative to the light enclosed within a radius

https://doi.org/10.1017/pasa.2019.23 Published online by Cambridge University Press

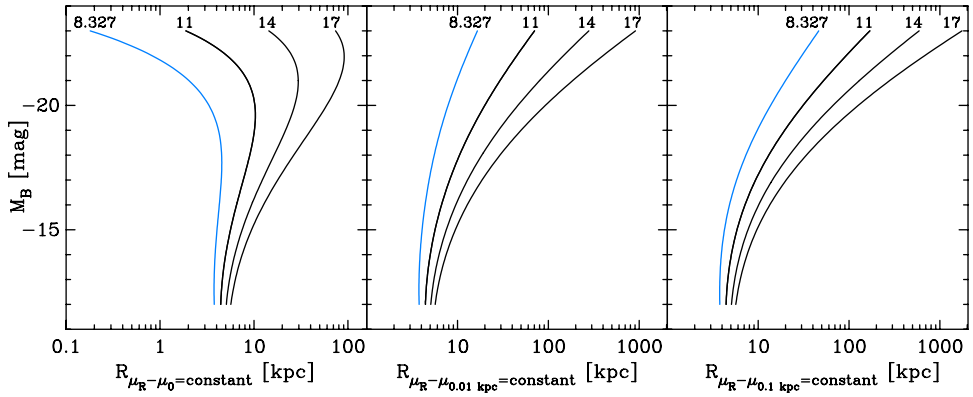

Figure 6. Left panel: Relations between the absolute B-band magnitude, $\mathfrak{M}_B$, and the radius where the associated light profile's surface brightness has dropped by a fixed amount from the central $R = 0$ value μ_0 (equation (17)) of the Sérsic model having a Sérsic index n dictated by the value of $\mathfrak{M}_B$ (equation (16)). The leftmost curve in each panel shows the result when using $\Delta\mu = 8.327$ mag arcsec^{-2}, which is the difference in surface brightness between μ_0 and μ_e of de Vaucouleurs' $R^{1/4}$ model. Middle panel: Similar, except that the radii shown here denote where the surface brightness profile has dropped by the same set of constant values used in the left panel, but now starting from $R = 0.01$ kpc rather than from $R = 0$. This helps to bypass the rapidly rising inner light profile of systems with high values of n, but which typically contain depleted cores. Right panel: Similar to the middle panel but starting from $R = 0.1$ kpc.

of infinity, that is, the total light. One can, alternatively, define a radius where the intensity is an arbitrary fraction of the intensity at $R = 0$. In the case of the exponential galaxy light profile model, the parameter h denotes the scale length where the intensity has dropped by a factor of e ≈ 2.718. This subsection explores radii where the intensity of the $R^{1/n}$ model has dropped by fixed amounts, effectively replacing the variable e^{b_n} term in equation (13) with a constant.

For de Vaucouleurs' $R^{1/4}$ model (equation (1)), it was noted that the intensity at R_e is $e^{7.669} \approx 2141$ times fainter than the intensity at $R = 0$. This corresponds to a surface brightness which is 8.327 mag arcsec^{-2} fainter than the central surface brightness. It is informative to explore what the size–luminosity diagram looks like when using this alternative, but equally valid, measure of ETG size, that is, the radius where the surface brightness has dropped by a constant 8.327 mag arcsec^{-2}. This is done in Figure 6, where a few other constant values are also used.

The left panel of Figure 6 reveals little evidence for a divide at $\mathfrak{M}_B \approx -18$ mag between the so-called dwarf and ordinary ETGs. Had astronomers used the above system of radii, calibrated to the Sérsic model's central surface brightness (at $R = 0$), rather than calibrated to the Sérsic model's total luminosity (at $R = \infty$), then they might well have concluded that there is a dichotomy between bright and faint ETGs at $\mathfrak{M}_B \approx -20$ mag and speculated that different physical processes must be responsible for the formation of ETGs fainter and brighter than this absolute magnitude. Some astronomers may have even heralded the observation of partially depleted cores in ETGs more luminous than $\mathfrak{M}_B \sim -20.5 \pm 1$ mag — thought to have formed their spheroids from major dry merger events — as the explanation for the bend seen in this alternative luminosity–size diagram.

In case some readers might be entertaining the $\Delta\mu = 8.327$ mag arcsec^{-2} curve in the left-hand panel of Figure 6 as evidence for a division at $\mathfrak{M}_B \approx -20$ mag, additional measures of radii based on larger differences in surface brightness from the central surface brightness have been included. One can see that the location of the bend in the scaling relations shifts from a B-band magnitude of roughly −20 to −22 mag as one samples more of the galaxy light. Once again, this demonstrates that these bends are not revealing the existence of different physical processes operating at magnitudes brighter and fainter than the location of the bend. The whip around to smaller radii seen at bright magnitudes in the left-hand panel of Figure 6 is due to the rapidly rising (with decreasing radii), inner light profile of systems with high Sérsic indices. One can devise schemes to circumvent this (see the middle and right-hand panels), which may be desirable given the partially depleted cores in these galaxies which prevent such bright μ_0 values actually being realised. The monotonic size–luminosity relations in Figure 6, which do not use radii where the intensity has dropped by systematically different amounts as a function of luminosity (as occurs with R_e and R_z) reveal no grounds for segregating dwarf and giant ETGs at $\mathfrak{M}_B \approx -18$ mag.

The middle and right-hand panels of Figure 6 show the distribution of ETG sizes where their surface brightness profiles have dropped by the same values as those used in the left-hand panel, but starting the drop from a radius of 0.01 and 0.1 kpc, rather than from the central value.

4.3. Isophotal radii

Based on isophotal radii, the luminosity–size relation for ETGs was initially considered to be log-linear, that is, linear in log space, unifying dwarf and giant ETGs (e.g. Heidmann, 1967, 1969; Holmberg, 1969; Oemler, 1976; Strom & Strom, 1978), and it largely still is (e.g. Forbes et al., 2008, see their Figure 3; van den Bergh, 2008; Nair, van den Bergh, & Abraham, 2011). This section would therefore be somewhat incomplete if it did not include isophotal radii.

Using a photographic (Pg, i.e. blue filter, Vega mag system) surface brightness of 26.5 mag arcsec^{-2} to define galaxy diameters, Holmberg (Holmberg, 1969, see his Figure 9) reported a linear relation, with a slope of −6, between the absolute magnitude and the logarithm of the isophotal major axis diameter[n]. Using the major axis diameter of the isophote corresponding to a photographic surface brightness of 25 (Vega) mag arcsec^{-2}, Heidmann (1967, 1969: see also Fraser, 1977 and Bigay & Paturel, 1980) obtained a less steep slope of −4.75 for ETGs[o] in the $\mathfrak{M}$–(log R_{iso})

[n] Using 'cut-off' radii, Oemler (1976) also reported a log-linear luminosity–size relation unifying dwarf and giant ETGs.
[o] Heidmann (1967, 1969) reported a slope of 2.8 for spiral galaxies.

https://doi.org/10.1017/pasa.2019.23 Published online by Cambridge University Press

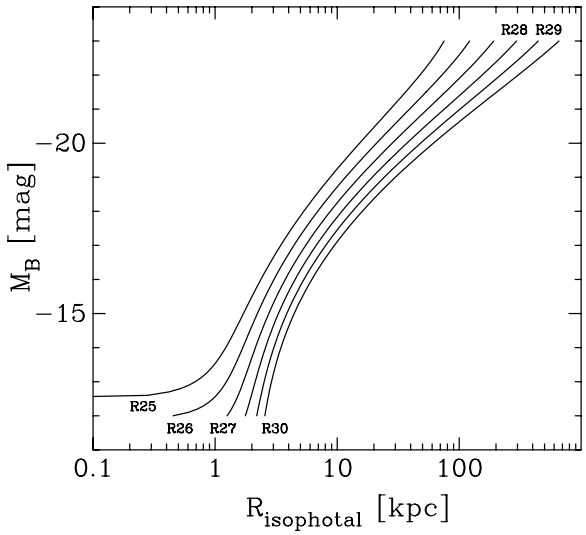

Figure 7. Six different isophotal radii are shown as a function of the *B*-band absolute magnitude (for which the typical Sérsic profile and Sérsic parameters are known from equations 16, 17, and 25).

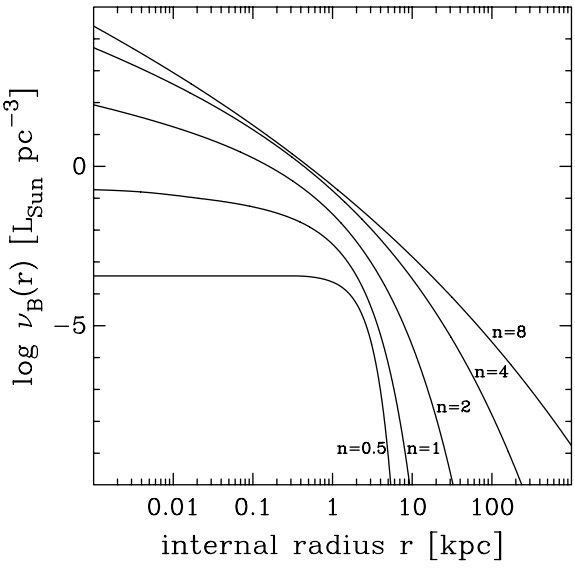

Figure 8. Internal, *B*-band, luminosity density profiles associated with the projected (surface luminosity density, i.e. surface brightness) profiles seen in Figure 2.

diagram, which he reported as a slope of 1.9 in the $\log L$–$\log R_{\rm iso}$ diagram.

Some half a century later, using the semimajor axis radius of the 3.6 μm isophote whose surface brightness equals 25.5 (AB) mag arcsec^{-2}, Muñoz-Mateos et al. (2015, see their Figure 14) presented a log-linear radius–(stellar mass) relation for different morphological types. The bright ETGs have the same slope as reported by Heidmann, with $\log M \propto (1.9 \pm 0.1) \log R_{3.6\mu{\rm m}=25.5}$. Approximating the low-luminosity end of the moderately curved L–$R_{\rm iso}$ relation with a power-law, the faint ETGs in Muñoz-Mateos et al. roughly follow a relation with a slope of 2.7 ± 0.2. Muñoz-Mateos et al. additionally show, in their Figure 15, that the use of $R_{\rm e}$, rather than isophotal radii, results in the strongly curved size–luminosity relation seen in Figure 4.

Figure 7 reveals what the size–luminosity relation for ETGs looks like when using six different isophotal radii (specifically, those radii where the *B*-band surface brightness equals 25, 26, ... 30 mag arcsec^{-2}) and using the total *B*-band absolute magnitude $\mathfrak{M}_B$ within a radius of infinite aperture. The smoothly changing slope is consistent with the slight curve observed for 50 years in magnitude-(isophotal radii) diagrams. For example, as noted above, a moderate change in slope is seen among the ETGs in the $\log \mathfrak{M}$–$\log R_{3.6\mu{\rm m}=25.5}$ diagram of Muñoz-Mateos et al. (2015) at 4–6 kpc. This can be understood in terms of the Sérsic index varying with absolute magnitude, which gives rise to the curves in Figure 7. Although it should be noted that the mapping between Figure 14 in Muñoz-Mateos et al. (2015) and Figure 7 shown here is not linear because of the colour–magnitude relation for ETGs (e.g. Ferrarese et al., 2006, see their Figure 123), in which fainter ETGs are bluer than luminous ETGs. To help anyone who may wish to explore this further, it is quickly noted that given that luminous ETGs have a $(B-3.6)$ colour of 4 to 5, the radius where the 3.6 μm surface brightness equals 25.5 mag arcsec^{-2} will roughly correspond to the $R_{B=30}$ isophotal radii seen in Figure 7, while ETGs with $\mathfrak{M}_B = -16$ mag have a $(B-3.6)$ colour of $\approx$2.5.

Past studies which did not include ETGs fainter than $\mathfrak{M}_B \approx -16$ mag could have missed the slight curvature in the L–$R_{\rm iso}$ diagram. The horizontal flattening of the curves associated with the brighter isophotal levels, seen at small radii in Figure 7, reflects that the central surface brightnesses in galaxies with these low absolute magnitudes is close to the isophotal value. Given that the ETGs in Figure 1 have $\mathfrak{M}_B < -13$ mag, the curves seen in Figure 7, and elsewhere, may not be reliable at $\mathfrak{M}_B > -13$ mag. At these low magnitudes, one encounters galaxies which may be a different, more heterogeneous class of galaxy with a broad range of colours (e.g. Jerjen et al. 2000; Hilker, Mieske, & Infante, 2003; Penny & Conselice, 2008).

5. Internal parameters

Projected quantities, such as those seen in the previous section, pertain to the line-of-sight column densities through a galaxy. To stave off criticisms that the analysis presented thus far needs to be performed using internal quantities, rather than projected fluxes and densities, this is now done.

The internal luminosity density profile, $\nu(r)$, can be computed from the observed, that is, the projected, intensity profile $I(R)$. Under the assumption of sphericity[p] $\nu(r)$ can be obtained by solving the following Abel integral (e.g. Binney & Tremaine, 1987):

$$\nu(r) = \frac{-1}{\pi} \int_r^\infty \frac{dI(R)}{dR} \frac{dR}{\sqrt{R^2 - r^2}}. \qquad (26)$$

For the Sérsic $R^{1/n}$ profile, $I(R)$, one has that

$$\nu(s) = \frac{I_{\rm e} e^b}{R_{\rm e}} \frac{b^n x^{1-n}}{\pi} \int_0^1 \frac{1}{t^2} \frac{\exp(-x/t)}{\sqrt{t^{-2n} - 1}} dt, \qquad (27)$$

where $s = r/R_{\rm e}$, $x = bs^{1/n}$, and t is the dummy variable (Ciotti, 1991; Graham & Colless, 1997). In passing, it is noted that Prugniel & Simien (1997) provide a useful parameterised model which approximates this, while Terzić & Graham (2005, see also Terzić & Sprague, 2007 for triaxial models) provide a modified expression with a power-law core.

Figure 8 shows the internal luminosity density profiles pertaining to the (projected) Sérsic light profiles displayed in Figure 2.

[p]This may not be particularly attractive given the bulge/disc nature of ETGs, but it offers some insight. Moreover, this approach should be roughly applicable to bulges, which are nowadays similarly misdiagnosed in structural scaling diagrams.

https://doi.org/10.1017/pasa.2019.23 Published online by Cambridge University Press

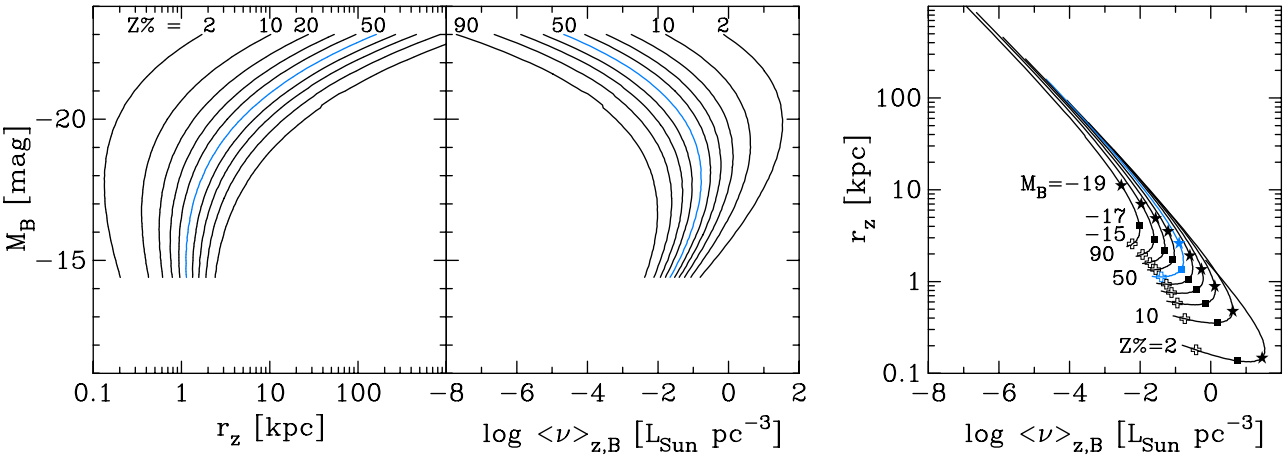

Figure 9. For a range of absolute *B*-band magnitudes with Sérsic indices $n > 1$, the internal radius r_z enclosing a sphere with Z percent of the total light is shown (left panel), as is the mean luminosity density $\langle\nu\rangle_z$ within this radius (middle panel: a somewhat similar pattern exists when using the internal luminosity density ν_z at r_z). The right-hand panel shows the log r_z–log$\langle\nu\rangle_z$ relations for fractions $Z = 2, 10, 20, 30, ...90\%$. The over-lapping nature of the relations for the brighter galaxies is the reason behind the tight log r_z–log ν_z relation discovered by Graham et al. (2006).

A solar absolute magnitude $\mathfrak{M}_{\odot,B} = 5.44$ mag was used (Mann & von Braun, 2015). For Sérsic indices $n < 0.5$, the internal density profile is known to have a central dip.

5.1. Internal effective radii

Subsection 4.1 explored parameters arising from projected radii, R, that effectively enclosed different percentages, Z, of the total galaxy light. Here, we explore parameters arising from internal radii, r, defining spheres which effectively enclose different percentages of the total galaxy light. Trends with these internal radii r_z, the average luminosity densities $\langle\nu\rangle_z$ contained within the spheres defined by these radii[q], and the absolute magnitude are investigated. The results can be seen in Figure 9.

As with the projected effective parameters, the internal effective parameters display a similar behaviour of strongly curved relations, in which the midpoint of each curve depends on Z and therefore obviously does not reflect a separation based on physically different formation processes. The midpoint of the bend shifts from roughly −19 to −16 mag as Z changes from 2 to 90%. A value of $Z = 50$ corresponds to the internal half-light radius r_e and the mean luminosity density $\langle\nu\rangle_e$, traced by the $Z = 50$ curves in Figure 9. The similarity between the $Z = 50$ curve in the left-hand panel of Figure 9 and the $Z = 50$ curve in the left-hand panel of Figure 4 was expected, given that $r_e \approx 4/3R_e$ (Ciotti, 1991). In addition, the similar patterns seen in both panels means that the different ratio of radii (r_{z_1}/r_{z_2}) at fixed absolute magnitude, for different percentages z_1 and z_2, will result in $\sigma^2 r/G$ mass estimates that depend on the percentage used to define r. As was seen in the middle panel of Figure 4, the ratio of radii again increasingly varies as the luminosity increases. This also coincides with an increased steepening of the velocity dispersion profile, impacting estimates of the dynamical mass (e.g. Wolf, 2011 Wolf et al., 2010; Forbes et al., 2011, see their Section 9.2) and further undermining the use of $\sigma^2 r_e/G$ in the brighter, non-dwarf, ETGs.

The right-hand panel of Figure 9 reveals that one can expect a strong log r_e–log$\langle\nu\rangle_e$ relation for bright ETGs. This is because if one mis-measures the internal radius enclosing 50% of the light and obtains a radius containing say 20 or 80% of the total light, the associated mean luminosity density that one measures will largely shift one along the log r_e–log$\langle\nu\rangle_e$ relation for bright ETGs (see also Trujillo et al., 2001, their Section 4). At low luminosities, faint of the midpoint of the bend in these curved relations, the same such mis-measurement will move one away from the curved log r_e–log$\langle\nu\rangle_e$ relation. This behaviour can be seen in the log r_e–log ν_e diagram of Graham et al. (2006, see their Figure 2b).

The collective broadening that can be seen at faint absolute magnitudes in the right-hand panel of Figure 9 can be compared with the right-hand panel of Figure 5. Note that Figure 9 only shows data for light profiles with $n > 1$ ($\mathfrak{M}_B < -14.3$ mag). Also bear in mind that the mean surface brightness (Figure 5) is 2.5 times the logarithm of the mean intensity, hence the greater range along the $\langle\mu\rangle_e$ axis in Figure 5 than compared to the log$\langle\nu\rangle_z$ axis in Figure 9.

5.2. Alternative internal radii

Similar to Subsection 4.2, we can explore the internal radii r where the internal density, ν, has dropped by a fixed amount from the value at some inner radius. Figure 8 reveals that, for Sérsic indices $n > 0.5$–1, the internal density profile rises steeply with decreasing radius. In the middle and right-hand panels of Figure 6, this rapid brightening of the projected surface brightness was circumvented by starting from the radius $R = 0.01$ and 0.1 kpc. Here, we start at $r = 0.01$ and 0.1 kpc to compute the internal radii where the internal luminosity density profile has dropped by a fixed amount from the density at these two inner radii. Figure 10 shows these alternative scale radii as a function of the absolute *B*-band magnitude (for magnitudes corresponding to $n > 1$). The relations seen there do not support an ETG divide at $\mathfrak{M}_B \approx -18$ mag.

5.3. Isodensity radii

Isodensity radii define a two-dimensional surface, such as a sphere, within a three-dimensional space. These radii are the internal analog to the projected isophotal radii seen in Subsection 4.3 and are naturally considered a better measure to define the radii of three-dimensional stellar systems. This is simply because isophotes

[q]A similar pattern (not shown in order to minimise repetitive figures) occurs when using the internal luminosity density, ν_z, at the internal radius, r_z.

https://doi.org/10.1017/pasa.2019.23 Published online by Cambridge University Press

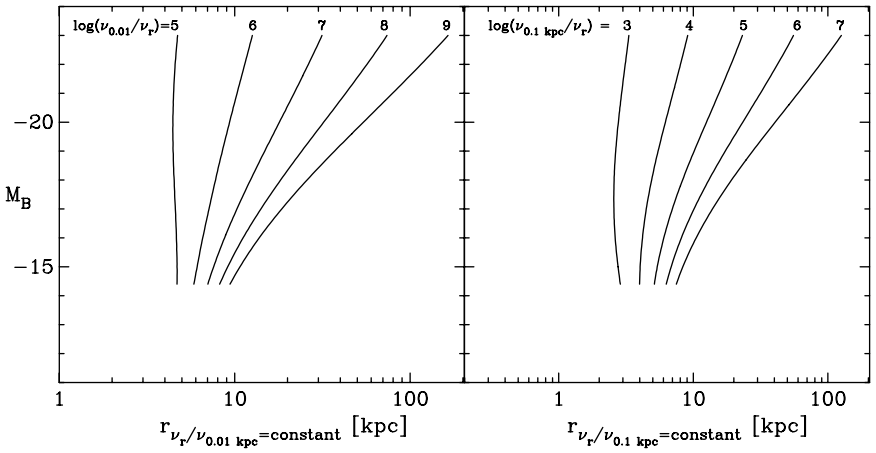

Figure 10. For each absolute magnitude, $\mathfrak{M}_B$, one can see the internal radius where the logarithm of the luminosity density (ν, in units of $L_{\odot,B}$ pc^{-3}) has decreased by a fixed amount from its value at $r = 0.01$ kpc (left panel) and $r = 0.1$ kpc (right panel).

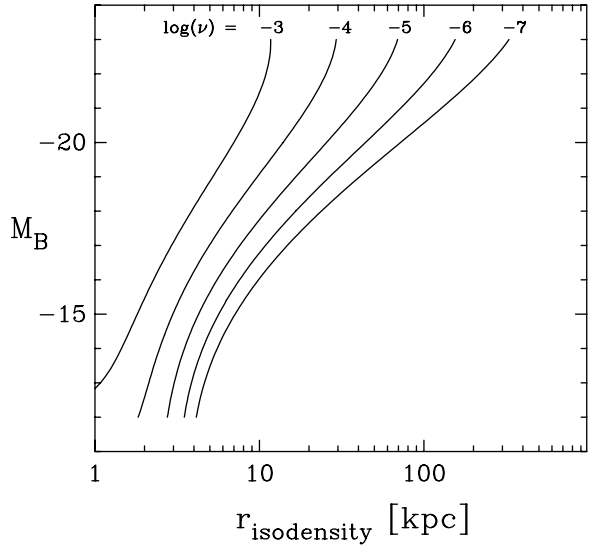

Figure 11. For each absolute magnitude, $\mathfrak{M}_B$, one can see the internal radius where the logarithm of the luminosity density (ν, in units of $L_{\odot,B}$ pc^{-3}) equals one of the five different values.

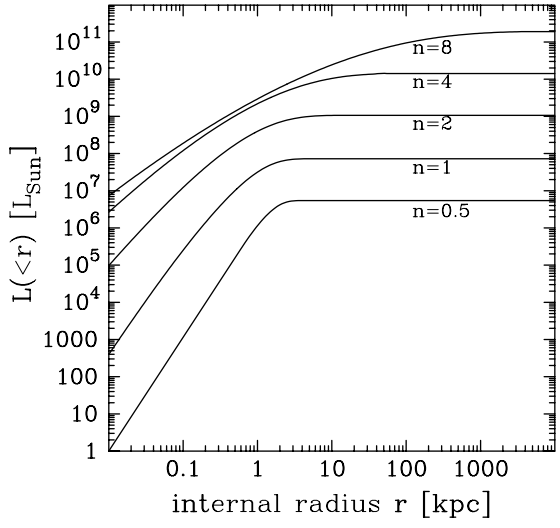

Figure 12. Representative, cumulative luminosity profiles for different Sérsic indices n, as matched to the light profiles shown in Figure 2.

can display an artificial (not physical) contour, arising from the projected column density through a galaxy, rather than a real boundary of equal density.

Figure 11 displays the $\mathfrak{M}_B$–$R_{\rm isodensity}$ relations for five different luminosity densities. The trends reveal no evidence for a divide at $\mathfrak{M}_B \approx -18$ mag.

While this concludes the recapitulation of the previous section but performed using internal parameters, it would be somewhat incomplete to proceed without having used the virial radii which are popular among theorists. Therefore, the following subsection presents this, along with an observer-inspired variation.

5.4. Virial radii

The integrated luminosity, within spheres centred on a galaxy, is given by

$$L_n(s) = I_{\rm e} e^b R_{\rm e}^2\, 4\pi \int_0^s \nu_n(s') s'^2 ds', \qquad (28)$$

and is shown in Figure 12 for our representative set of profiles from Figure 8.

Multiplying by a stellar mass-to-light ratio gives the cumulative stellar mass profiles. The luminosity density profiles $\nu(r)$ (equation (27)) were converted into stellar mass density profiles $\rho(r)$, using a constant B-band stellar mass-to-light ratio of $M/L_B = 8$.

Following Macciò, Murante, & Bonometto (2003, their equation 1.1; see also Bryan & Norman, 1998), a proxy[r] is used for the virial radius defined as the radius of the sphere within which the average (stellar mass) density is equal to $18\,\Pi^2\,\Omega_{\rm matter}^{0.45}\,\rho_{\rm critical} \approx 177.7 \times 0.589 \times \rho_{\rm critical} \approx 104.6\,\rho_{\rm critical} \approx (339.5\ \Omega_{\rm matter})\,\rho_{\rm critical}$. The Planck 2015 results (Planck et al., 2016) give $\Omega_{\rm matter} = 0.308 \pm 0.012$ and thus $339.5\,\Omega_{\rm matter} = 104.6$. They also report $H_0 = 67.8 \pm 0.9$ km s^{-1} Mpc^{-1} and thus $\rho_{\rm critical} \equiv 3H_0^2/(8\Pi G) = 0.864 \times 10^{-26}$ kg m^{-3}, or 39.3 M$_\odot$ kpc^{-3}. The popular, and smaller, r_{200} radius (Carlberg, Yee, & Ellingson, 1997), within which the average (stellar mass) density is equal to

[r] Zemp (2014) explains why this is a proxy for the virialised region. Moreover, only the stellar mass for this alternate measure of galaxy size is considered here.

https://doi.org/10.1017/pasa.2019.23 Published online by Cambridge University Press

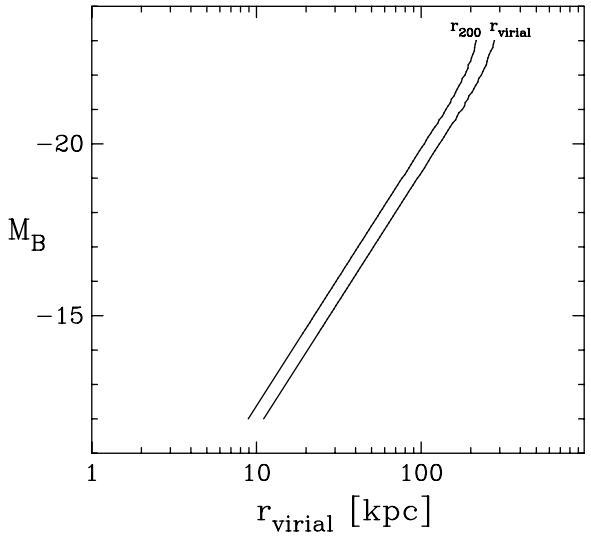

Figure 13. The virial radius is shown as a function of the *B*-band absolute magnitude $\mathfrak{M}_B$. The average stellar mass density within the virial radius equals 104.5 $\rho_{\rm critical}$. Also shown is the radius r_{200} within which the average density equals $(200/\Omega_{\rm matter})\rho_{\rm critical}$. The slope equals −3, except for the luminous galaxies with high Sérsic indices, and thus long tails to their light profiles, with stars beyond the virial radius.

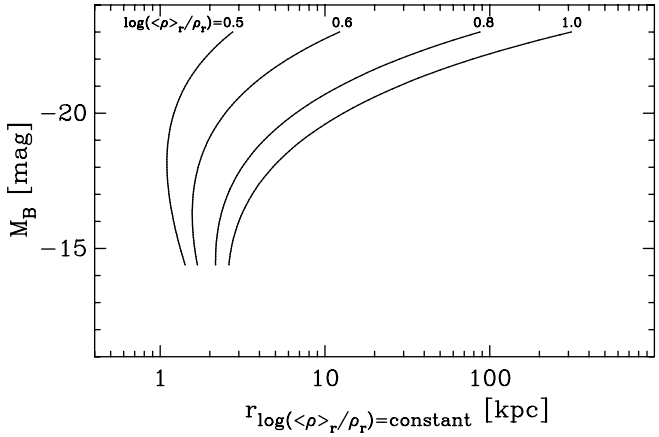

Figure 14. Internal radius where the mean enclosed density equals some fraction of the density at that radius.

$200\rho_{\rm critical}$, is additionally calculated. The virial radius and the r_{200} radius (associated with the stellar mass and thus ignoring any potential dark matter halo) is shown in Figure 13 as a function of the absolute magnitude[s].

For $\mathfrak{M}_B \gtrsim -22$ mag, the slope of the $\mathfrak{M}_B$–$r_{\rm virial}$ and $\mathfrak{M}_B$–r_{200} relation is 7.5. Converting the magnitude axis to log (luminosity) and applying a constant stellar mass-to-light ratio (as was assumed for calculating the virial radii) would give a slope of $7.5/2.5 = 3$ for the logarithmic mass–size relation. Thus, for $\mathfrak{M}_B \gtrsim -22$ mag, the radii are large enough that they enclose the bulk of the stellar mass M, and thus, the pursuit of a constant, average enclosed density (mass/volume) is simply giving radii that meet the condition $M \propto r^3$. As such, the masses may as well be point masses, as the information in the density profile is effectively lost.

5.4.1. A variation

Here, a new internal galaxy radius, $r_{\rm g}$, is introduced. It is such that the average density within this radius equals some fraction of the local density at that radius. Mathematically, this can be thought of as a variation of the virial radius, which can be expressed as

$$\log(104.6) = \log\langle\rho\rangle_{r_{\rm virial}} - \log\rho_{\rm critical}. \quad (29)$$

The variation introduced here can be written as

$$\log({\rm H}) = \log\langle\rho\rangle_{r_{\rm g}} - \log\rho(r = r_{\rm g}). \quad (30)$$

This radius is somewhat akin to Petrosian (1976) radii, used by observers, which is such that the average intensity within some projected radius $R_{\rm P}$ divided by the intensity at that radius (denoted η) equals some constant value, typically 5 (e.g. Bershady, Jangren, & Conselice 2000; Blanton et al., 2001). For Petrosian radii, one has the expression

$$-2.5\log[\eta = 5] = \langle\mu\rangle_{R_{\rm P}} - \mu(R = R_{\rm P}) \quad (31)$$

Figure 14 presents these new galaxy radii (equation (30)) for values of $\log {\rm H} = 0.5$, 0.6, 0.8, and 1.0. One can see that they, unlike the virial radii, are no longer too large to be unaffected by the galaxies' structure. They behave in a fashion somewhat similar to the internal radii containing different fractions of the galaxy light. Once again, no convincing evidence for a dichotomy at a fixed magnitude is apparent.

6. Case studies

Graham & Guzmán (2003) compiled data for ∼250 ETGs to demonstrate the unified nature of dwarf and ordinary ETGs across the alleged divide at $\mathfrak{M} \approx -18$ mag. This data set included *Hubble Space Telescope* (*HST*)-resolved dwarf ETGs plus *HST*-resolved, ordinary, ETGs from Faber et al. (1997), among which those ETGs without depleted cores followed the $\mathfrak{M}$–μ_0 relation (equation (17)). Since then, a few additional ETG data sets have come forth, and it is insightful to elaborate on alleged discrepancies or differences using two of these.

6.1. Case study 1: Ferrarese et al. (2006)

Ferrarese et al. (2006) imaged 100 Virgo cluster ETGs with *HST* and the F475W filter (transformed to the AB photometric system's *g*-band) as a part of the 'Advanced Camera for Surveys Virgo Cluster Survey' (ACSVCS; Côté et al., 2004; Ferrarese et al., 2006). Ferrarese et al. (2006) fit seeing-convolved Sérsic and core-Sérsic models (plus optional nuclear excesses) to the (geometric mean)-axis[t] surface brightness profiles. As such, because they take the ellipticity profile into account, their models can be readily integrated to obtain the total galaxy magnitude. The (surface brightness fluctuation)-based distances from Mei et al. (2007) have been used to convert these model magnitudes into absolute magnitudes, and they have been corrected for Galactic extinction using the values from Schlafly & Finkbeiner (2011), as tabulated in the NASA/IPAC Extragalactic Database (NED)[u].

[s]Although Kravtsov (2013, see also Huang et al., 2017) reports an approximately linear $r_{\rm e}$–r_{200} relation, apparently at odds with the results in Figure 13 and the left panel of Figure 9, it needs to be remembered that his relation based on 'abundance matching' of simulated dark matter halos with stellar mass estimates of real galaxies uses an r_{200} that pertains to the dark matter halos. As such, it is therefore not equivalent to the r_{200} used here and is thus not at odds with the results reported here.

[t]Geometric mean of the major- and minor-axis.
[u]http://nedwww.ipac.caltech.edu

https://doi.org/10.1017/pasa.2019.23 Published online by Cambridge University Press

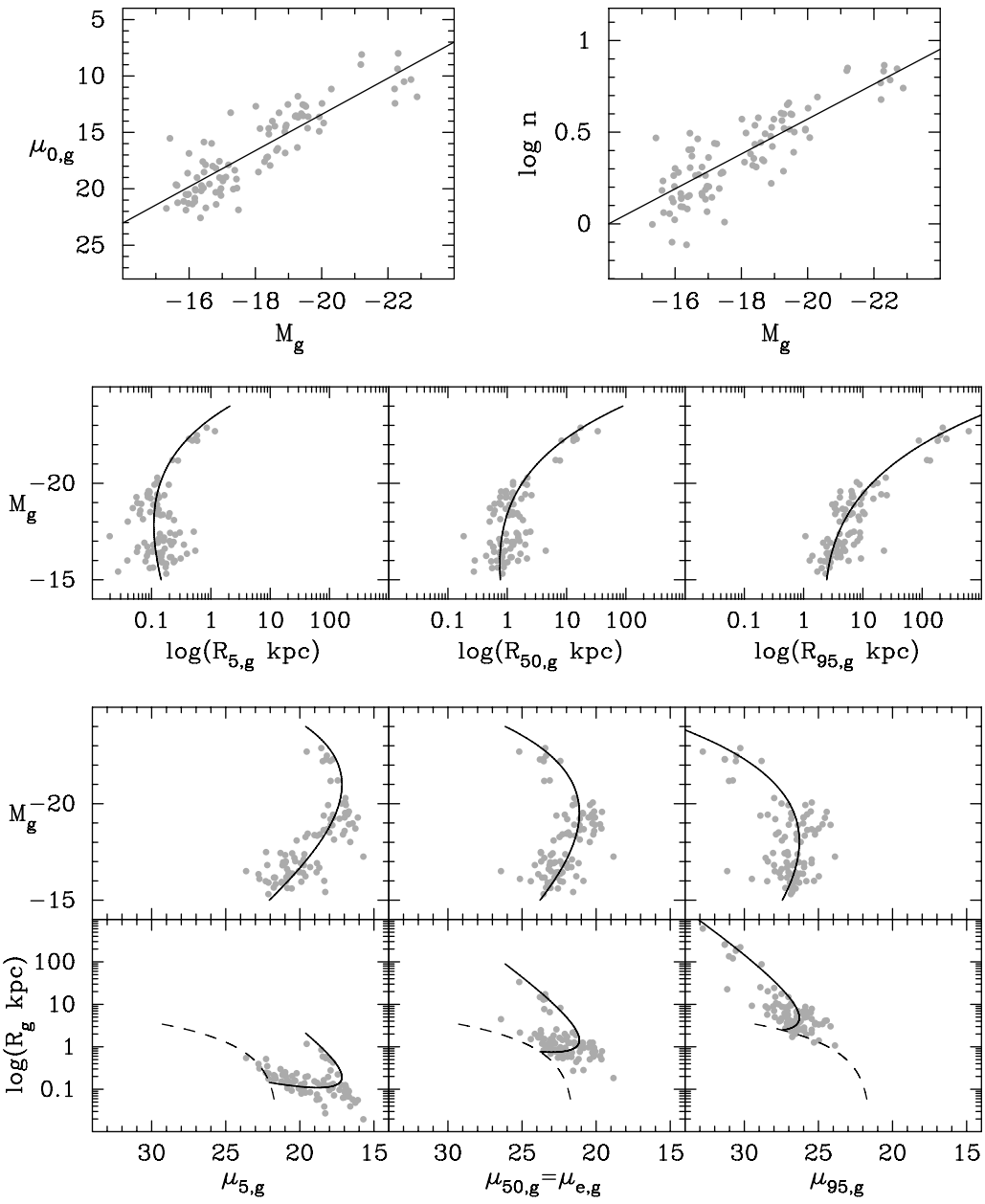

Figure 15. Sample of 94 Virgo cluster ETGs from Ferrarese et al. (2006). Top row: The Sérsic parameters, including $\mathfrak{M}_g$ and $\mu_{0,g}$, are from fits to the (geometric mean)-axis light profiles. The lines are defined in equations 32 and 33. Middle and bottom rows: The solid curves are predictions based on the linear fits in the top panels. The three equal-dashed curves in the lower panels show the $\mathfrak{M}_g = -15$ mag boundary. Looking at the two lower left-hand panels, one might be inclined to call for a divide at $\mathfrak{M} = -20.5 \pm 0.5$ mag, while looking at the two lower right-hand panels, one may instead be inclined to advocate for a divide at $\mathfrak{M} = -18 \pm 1$ mag.

Of these 100 galaxies, 2 (VCC 1535; VCC 1030) could not be modelled by Ferrarese et al. (2006) due to dust, and 2 (VCC 1250 and VCC 1512) have core-Sérsic fits which Ferrarese et al. (2006, see their Section 4.2) discredit — and rightfully so given that the R_e values hit their limit of 490 arcsec, as was also the case for VCC 575 ($\mathfrak{M}_B = -17.61$ mag). In addition to these five galaxies, the S0 galaxy VCC 1321 (NGC 4489, $\mathfrak{M}_B = -18.20$ mag) which was reported to have an unusually high galaxy Sérsic index of $\sim$6 (cf. 2.3 ± 0.5 from Table C1 of Krajnović et al., 2013) is also excluded.

Here, we will see how the linear $\mathfrak{M}$–μ_0 and $\mathfrak{M}$–n relations[v], spanning the Virgo ETG sample's full magnitude range, explain the curved trends in diagrams involving effective radii and effective surface brightnesses. The following two g-band equations approximate the distribution of data seen in the upper panels of Figure 15:

$$\mathfrak{M}_g = -10.5 \log(n) - 14.0, \text{ and} \quad (32)$$

$$\mathfrak{M}_g = 0.63\mu_{0,g} - 28.4, \quad (33)$$

The predicted g-band $\mathfrak{M}$–μ_z and $\mathfrak{M}$–R_z distributions are presented in the middle and lower panels of Figure 15 for $z = 0.05, 0.5$, and 0.95. Similar results are obtained with the $\mathfrak{M}$–$\langle\mu\rangle$ diagram and also when using their data obtained through the F850LP filter.

The middle and lower panels of Figure 15 should be compared with Figure 117 in Ferrarese et al. (2006), which used quantities at $z = 0.05$ and 0.5 ($Z = 5\%$ and 50%), and compared with Figure 76

[v]Equations 27 and 30 in Ferrarese et al. (2006) are similar to equations 16 and 17 but are a blend of B-band data and g-band data on the AB photometric system.

https://doi.org/10.1017/pasa.2019.23 Published online by Cambridge University Press

in K09 which used quantities at 50%. The series of linear equations 17– 26 in Ferrarese et al. (2006) — used to approximate the bright and faint ends of their $\mathfrak{M}$–μ_e, $\mathfrak{M}$–R_e, $\mathfrak{M}$–μ_5, and $\mathfrak{M}$–R_5 distributions — does not adequately capture the curved nature of the scaling relations which unify the faint and bright ETGs in these diagrams. Their equations have been fit separately to the core-Sérsic and Sérsic galaxies, implying a division between these two galaxy types in these diagrams. However, their set of linear approximations are not only dependent upon the magnitude range included in the fit, but they go against the premise of a continuity in these diagrams and against the understanding that the different slopes at bright and faint magnitudes cannot be used to interpret signs of different galaxy types or formation physics in diagrams involving 'effective' parameters. Ferrarese et al. (2006) understood that there is a continuity at $\mathfrak{M} = -18$ mag and a divide at $\mathfrak{M} \approx -20.5$ mag — as did Gavazzi et al. (2005); Côté et al., 2007, 2006; Misgeld, Mieske, & Hilker, 2008 2009; and Chen et al., 2010 — but diagrams involving effective radii and effective surface brightnesses can not be used to make this diagnosis. Similarly, the colour-coding used by K09 (see their Figure 76) is inappropriate and misleading.

6.2. Case study 2: Kormendy et al. (2009)

K09 accept[w] the $\mathfrak{M}$–n relation (see their Figure 33) but they deny the existence of a linear $\mathfrak{M}$–μ_0 relation unifying dwarf and ordinary ETGs (see their Figure 1). This follows on from Kormendy (1985, see his Figure 3), which produced an $\mathfrak{M}_B$–μ_0 diagram with a sample selection that had an absence of ETGs with magnitudes $-17 \gtrsim \mathfrak{M}_B \gtrsim -20.5$ mag ($H_0 = 50$ km s^{-1} Mpc^{-1}), making it difficult to know where a transition may occur.[x] Further complicating the situation was that the faint ETG data in Kormendy (1985) did not produce the known $\mathfrak{M}_B$–$\mu_{0,B}$ trend (e.g. Binggeli et al. 1984, see their Figure 8)[y] whose distribution points towards the *faint*-end of the $\mathfrak{M}_B$–$\mu_{0,B}$ sequence for bright ETGs with depleted cores. That is, according to the data in Kormendy (1985), the ETGs fainter than $\mathfrak{M}_B \approx -17$ mag follow a distribution with a steeper slope in the $\mathfrak{M}_B$–$\mu_{0,B}$ diagram than shown in the right-hand panel of Figure 1, such that the distribution of faint ETGs in Kormendy (1985) points to the *bright*-end of the distribution of ETGs with depleted cores. Despite the ongoing rejection by K09 for a unifying $\mathfrak{M}$–μ_0 relation across $\mathfrak{M}_B = -18$ mag ($\mathfrak{M}_{V_T} \approx -19$ mag), K09 did not actually show the $\mathfrak{M}$–μ_0 diagram for their data set nor the $\mathfrak{M}$–μ_5 diagram used by Ferrarese et al. (2006).

K09 also excluded many of the ETGs in Ferrarese et al. (2006) because they wanted to work with what they thought was a sample of predominantly one-component galaxies, that is, no lenticular galaxies. K09 effectively thinned-out much of the population of ETGs from $-18 > \mathfrak{M}_B > -20.5$ mag. This resulted in a sample of 42 ETGs, including 10 dwarf ETGs. However, 5 of the 32 non-dwarf galaxies were subsequently identified as S0 galaxies by K09. Furthermore, another 5 were rare compact elliptical (cE) galaxies, taken from Table XIII of Binggeli et al. (1985; who note in Part 3 of their Appendix that the M32-like galaxies are vastly outnumbered by dwarf ETGs of similar magnitude: $-14 > \mathfrak{M}_B > -18$ mag). The cE galaxies are thought to be heavily stripped disc galaxies (e.g. Rood, 1965; Bekki et al., 2001; Graham, 2002*b*; Chilingarian et al., 2009), while the isolated cE galaxies may have either never acquired a significant disc or may have been ejected from a cluster after losing much of their disc (e.g. Chilingarian & Zolotukhin, 2015). The cE galaxies are two-component systems, likely dominated by a remnant bulge, and are known to overlap with the bulges of spiral and S0 galaxies in the scaling diagrams (e.g. Graham 2013, see his Figure 1). This over-representation of cE galaxies, relative to normal galaxies, in K09 is inappropriate for two reasons. In terms of a sample providing a balanced representation of galaxies, there should be ∼200 times (I. Chilingarian 2018, priv. comm.) fewer cE galaxies than non-cE galaxies across their co-existing range in absolute magnitude. Second, the cE galaxies are more akin to bulges, and as such, they are better compared with bulges than with parameters from single Sérsic fits to ETGs that typically contain bulges and discs.

As for the five galaxies identified by K09 as lenticular galaxies, K09 performed a bulge/disc decomposition for these. As with their fitting of a single Sérsic model, they did not convolve their models with the central image's point spread function but excluded by eye the region they considered to be affected by either nuclear excesses or a partially depleted core. They then used the *bulge* parameters rather than the *galaxy* parameters for these 5 galaxies to compare with the *galaxy* parameters of the remaining galaxies which they thought were pressure-supported, single-component systems (with additional small nuclear excesses or cores). However, Emsellem et al. (2011, see their Table B1) report on the internal kinematics for the brightest 19 of the supposed 27 (= 32 − 5) 'elliptical' galaxies in K09. They reveal that 10 of these 19 are 'fast rotators', and Krajnović et al. (2013) provide bulge/disc decompositions for 7 of them. Furthermore, Toloba et al. (2015) contains internal kinematical information for 6 of the 10 'dwarf spheroidal' galaxies in K09, reporting that 4 of these 6 are 'fast rotators'. K09 have therefore plotted a mixture of bulge parameters (for 5 S0 galaxies) and galaxy parameters (for at least 11, and likely more, S0 galaxies). This blurs prospects for identifying connections in parameter scaling diagrams, and it explains why K09 did not find the known $\mathfrak{M}$–n or $\mathfrak{M}$–μ_0 relations. Given that bulges and ETGs follow a different size–luminosity relation, they cannot follow the same $\mathfrak{M}$–n and $\mathfrak{M}$–μ_0 relations (see 4.1). The $\mathfrak{M}$–n diagram in K09 is thus a blurring of two distributions, which have been separated here in Figure 16.

The upper panels in Figure 16 display the $\mathfrak{M}$–μ_0 (Vega V-band mag) diagram using the data from K09. One can see that there is an $\mathfrak{M}$–μ_0 relation for ETGs, although a couple of high−n ETGs appear to have had their Sérsic index over-estimated and their total magnitudes under-estimated[z] by the (roughly) isophotal magnitudes advocated by K09 and used here for comparative purposes.

[w] While K09 acknowledge the $\mathfrak{M}$–n relation, they claim that it is insensitive to the formation physics of ETGs because there is no discontinuity at $\mathfrak{M}_B \approx -18$ mag. The abstract of K09 also claims that there is no $\mathfrak{M}$–n correlation for the core-Sérsic galaxies and almost no correlation for the Sérsic galaxies.

[x] Graham (2005) presented the Virgo cluster Luminosity Function for ETGs (with data provided courtesy of H. Jerjen, priv. comm.). It showed no evidence of a division. More recently, Ferrarese et al. (2016, see their Figure 4) reviewed the luminosity function for all galaxy types in the core of the Virgo cluster. A small dip is evident at $M_B = -17$ mag, which could disappear upon rebinning the histogram.

[y] Kormendy & Djorgovski (1989) addressed this issue in a footnote, by (incorrectly) claiming that seeing effects on dwarf galaxies contributed to the continuity seen by Binggeli et al. (1984) and others.

[z] NGC 4552 (VCC 1632) is one of these high-n galaxies, with a reported major-axis Sérsic index equal to 9.22 (K09) and a (geometric mean)-axis Sérsic index equal to 7.6 (Ferrarese et al., 2006). Bonfini et al. (2018) reassign NGC 4552 from a core-Sérsic galaxy type to a Sérsic galaxy given that its 'core' is due to dust and, after accounting for interloping/undigested galaxy flux, Sahu, Graham, Davis, 2019 measure Sérsic indices, from Spitzer 3.6 μm images, equal to 5.42 and 5.36 for the major-axis and (geometric mean)-axis, respectively. Krajnović et al. (2013) report a Sérsic index of 6.2 for this galaxy. Krajnović et al. also report indices of 5.5 and 2.9 for NGC 4406 and NGC 4486, respectively (cf. 10.27 and 11.84 in K09, who offer reasons in their Section 7.5 for why they may have obtained their unusually high Sérsic index for NGC 4406). Their high Sérsic index

https://doi.org/10.1017/pasa.2019.23 Published online by Cambridge University Press

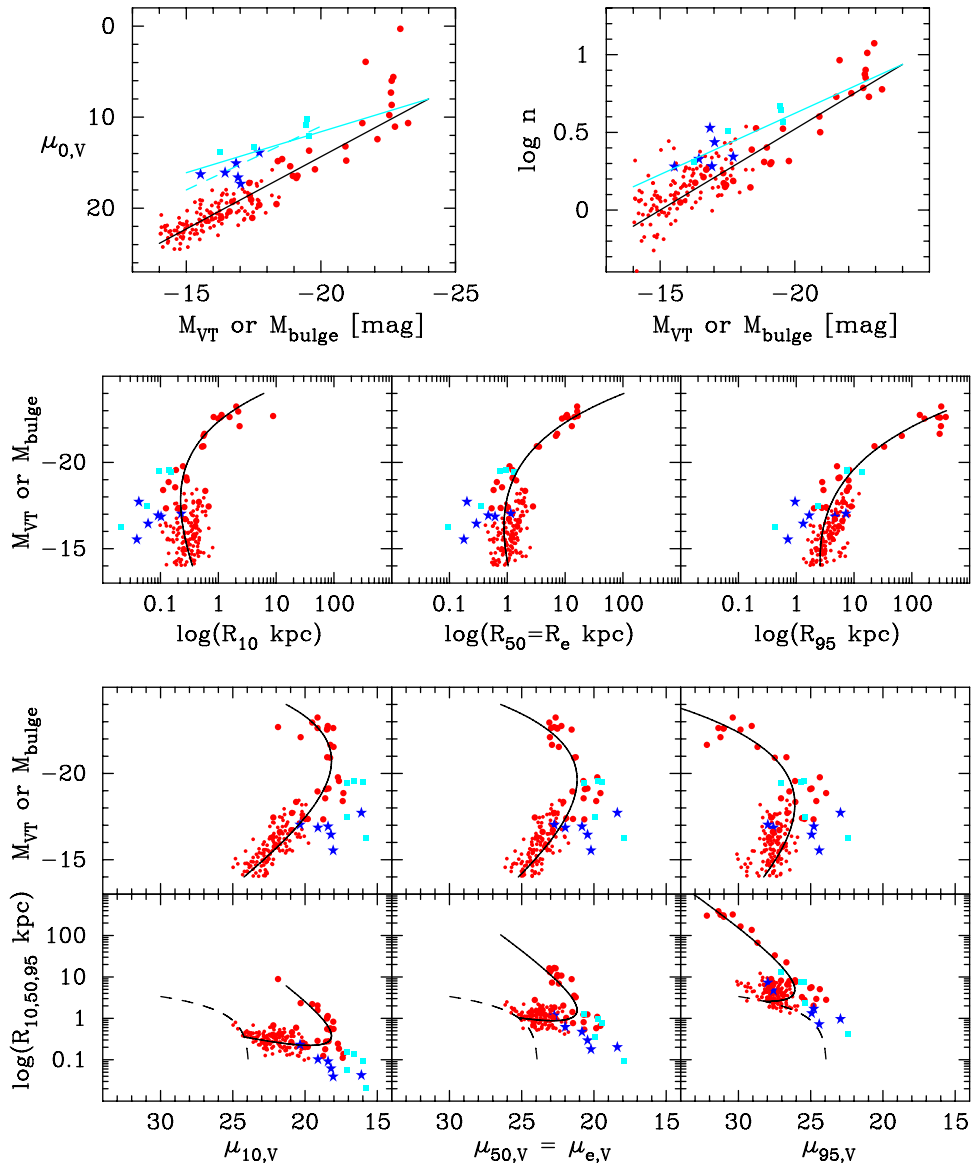

Figure 16. Sample of 42 stellar systems in the Virgo cluster from K09, comprising ordinary ETGs (large red circles), 5 bulges of ETGs (light blue squares, NGC: 4570, 4660, 4564, 4489, 4318), and 6 compact elliptical galaxies (dark blue stars, VCC: 1297, 1192, 1440, 1627, 1199, 1545) which are considered to be the remnant bulges of stripped disc galaxies. An additional 128 Virgo cluster 'dwarf' ETGs from Binggeli & Jerjen (1998) show the extension to fainter magnitudes. A rough $B-V=0.8$ colour was applied uniformly to this latter sample of B-band data. Top panel: The parameters are from Table 1 in K09, where the absolute magnitudes $\mathfrak{M}_{V_T}$ were derived independently of the Sérsic model for the ETGs and cE galaxies and are from their column 11; the Sérsic indices are major-axis values; and the central surface brightnesses are the $R=0$ values from their Sérsic models fit either to the galaxy or, in 5 instances, the bulge component. Expressions for the red ETG lines are provided in equations 34 and 35. Middle and lower rows: Similar to Figure 15. The three equal dashed curves show the $\mathfrak{M}_{V_T}=-14$ mag boundary. Neither the absolute magnitudes, effective half-light (50%) radii, nor effective surface brightnesses in the lower middle panels are from the Sérsic model but were instead obtained independently from 2D profile integration by K09. The 10% and 95% radii and surface brightnesses were derived from the Sérsic model.

The following equations represent the lines for ETG shown in the upper row of Figure 16.

$$\mathfrak{M}_{V_T} = -9.6\log(n) - 15.0, \text{ and} \quad (34)$$

$$\mathfrak{M}_{V_T} = 0.63\mu_{0,V} - 29.0. \quad (35)$$

As can be seen in Figure 16, the cE galaxies do not follow either the $\mathfrak{M}$–n nor the $\mathfrak{M}$–μ_0 relations for ETGs. The bulges of the S0 galaxies similarly do not follow these relations. For a given central surface brightness, the bulges have fainter absolute magnitudes than the ETGs, which makes sense given that their disc light has been excluded. The offset to fainter absolute magnitudes in the $\mathfrak{M}$–n diagram is not as great, due to the reduced Sérsic indices of these bulges relative to their galaxy Sérsic indices (which tend to be higher due to the outer disc light). K09 do not use a different colour to denote the (i) cE galaxies, (ii) bulges, and (iii) ETGs. This missing information makes it difficult to appreciate what is going on in their scaling diagrams.

K09 elected to plot the $\mathfrak{M}$–μ_{10}, rather than the $\mathfrak{M}$–μ_0 or $\mathfrak{M}$–μ_5, and the $\mathfrak{M}$–μ_e diagrams, which are shown here in Figure 16, along with the $\mathfrak{M}$–μ_{95} diagram, with the bulge- and galaxy-type information included. The exclusion of known S0

for NGC 4486 is likely due to the halo of intracluster light surrounding this cD galaxy (see Graham et al., 1996 and Seigar, Graham, & Jerjen 2007 to appreciate this).

https://doi.org/10.1017/pasa.2019.23 Published online by Cambridge University Press

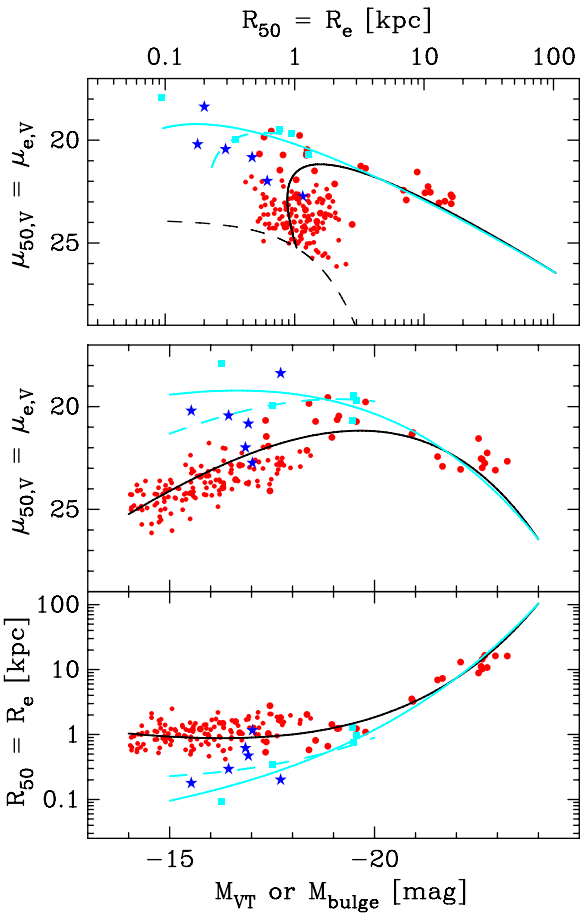

Figure 17. Zoom in and summary of the effective half-light parameters displayed in Figure 16. Here, the predicted relations for bulges — according to the two linear relations in Figure 16 — have also been included. This diagram facilitates comparison with, and understanding of, Figure 14 in Bender, Kormendy, & Cornell (2015) — where bright S0 galaxies were often either excluded or their *bulge* parameters plotted, and where dwarf S0 galaxies always have their *galaxy* parameters plotted.

galaxies by K09, coupled with their use of bulge rather than galaxy parameters for some S0 galaxies but not others, results in a thinning of the bridging population of ETGs around $\mathfrak{M}_B = -18$ to -20.5 mag in their diagrams. This practice is particularly apparent throughout Kormendy & Bender (2012), Bender et al., 2015, and Kormendy (2016). Furthermore, their attempted shift of focus to dynamically hot[aa] systems, i.e., the bulge sequence (e.g. Balcells et al., 2007; Graham, 2013, and references therein), rather than the ETG sequence, came at the expense of realising the continuous ETG sequence, that is, the continuity between dwarf and ordinary ETGs, and contributed to their ongoing belief in the artificial divide at $\mathfrak{M} \approx -18$ mag.

Figure 17 has been included to better help one evaluate the colour-coding and information presented in the scaling diagrams of K09, Bender et al. (2015), Kormendy (2016), and elsewhere. The curved distribution for the ETGs in these scaling diagrams involving the arbitrary 'effective' parameters is not a sign of division but arises from the unity seen in the $\mathfrak{M}$–μ_0 and $\mathfrak{M}$–n diagrams. As will be broached in 7.3, numerous other scaling relations also display a continuity across the alleged dwarf/ordinary ETG divide at $\mathfrak{M}_B = -18$ mag.[ab]

7. Discussion

7.1. $\mathfrak{M}$, μ_e, and R_e

Although Sérsic (1968*b*) plotted magnitude and mass versus R_e without yet fully appreciating the nature of ETGs[ac], that is, how ETG light profiles systematically change shape with absolute magnitude, Sérsic (1968*a*) provided the very tool, that is, the $R^{1/n}$ model[ad], that subsequently resulted in the realisation that the curved distribution of ETGs in diagrams using R_e, or the associated μ_e and $\langle\mu\rangle_e$, is a consequence of the continual change in the Sérsic index n with absolute magnitude.

Both Sérsic (1968*b*) and Fish (1963) deserve more recognition than received to date. Their (R_e-based size)-luminosity (and size-mass) relations are the linear approximation to the bright arm of the curved size–luminosity relation for ETGs (see Graham et al., 2006) that is still fit by countless papers today (e.g. Shen et al., 2003; Lange et al., 2015). As noted earlier, this linear approximation from half a century ago also simultaneously yields the linear approximation to the bright arm of both the $\langle\mu\rangle_e$–R_e relation and the μ_e–R_e relation, which later became known as the Kormendy (1977) relation after Kormendy was the first to plot μ_e versus R_e.

Like previous papers, Kormendy (1977) used de Vaucouleurs' $R^{1/4}$ model to parameterise the galaxy sample and wrote 'some experimentation suggests that the most relevant correlation is between B_{0V} [μ_e] and r_0 [R_e]' and that 'the interpretation of the $B_{0V}(\log r_0)$ [μ_e–$\log R_e$] is unknown'. As with Fish (1963), he had found that the *B*-band effective surface brightness was not constant among the ETG population. For luminous ETGs, Kormendy (1977) reported that $\mu_e \propto 3 \log R_e$ over a range of 3.5 mag arcsec^{-2}. Although the following papers did not fit a curved relation, the more complete curved distribution for ETGs can be seen in Kodaira et al. (1983), Ichikawa et al. (1986), and Capaccioli & Caon (1991; see also Binggeli et al., 1984 in regard to the curved $\mathfrak{M}_B$–$\langle\mu\rangle_e$ distribution). As interpretted/explained here, the μ_e–R_e and $\langle\mu\rangle_e$–R_e relations for bright ETGs are tight because ETGs with Sérsic $n \gtrsim 3$ have similar (near over-lapping) light profiles. As such, errors in R_e, and thus μ_e and $\langle\mu\rangle_e$, shift bright ETGs of a given magnitude along these near over-lapping light profiles, maintaining a μ_e–R_e and $\langle\mu\rangle_e$–R_e relation that resembles the μ–R and $\langle\mu\rangle$–R light profiles (see Figure 5).

We have seen why fainter ETGs, with progressively different light profiles, smoothly depart from the μ_e–R_e and $\langle\mu\rangle_e$–R_e relations for bright ETGs. Figure 5 reveals why Ichikawa et al. (1986) were mistaken when they interpreted the curved μ_e–R_e distribution, see their Figure 12, as strong evidence for a separation of dwarf and giant ETGs; and half of the answer as to why they were mistaken is evident in their linear $\mathfrak{M}_B$–concentration relation (see their Figure 11). However, they were in good company, following Michard (1979), and their data quality and trends appear accurate.

[aa] Due to the rotation of some classical bulges (e.g. Saha, Martinez-Valpuesta, & Gerhard, 2012), one may hesitate to call this a 'dynamically-hot' sequence for pure-elliptical galaxies and bulges. Sequences for bulges can be seen in Graham & Worley (2008) and Graham (2013).

[ab] Whether or not any type of sequence might unite three-dimensional ellipsoids, from nuclear star clusters and ultra-compact dwarf galaxies to bulges and pure-elliptical galaxies, does not undermine the continuity between dwarf and normal ETGs.

[ac] Sérsic (1968*b*) used $R^{1/4}$-model R_e for the ETGs, most of which he thought were elliptical galaxies.

[ad] Sérsic introduced the $R^{1/n}$ model to describe galaxies consisting of what he thought was varying ratios of $R^{1/4}$-bulge and exponential-disc.

https://doi.org/10.1017/pasa.2019.23 Published online by Cambridge University Press

It should also be borne in mind that any continuum can be split into two, but this does not mean that one has two distinct populations. For example, the colours of ETGs become more blue as one progresses to fainter magnitudes[ae] (e.g. Baum, 1959; Visvanathan & Sandage, 1977; Driver et al., 2006; Lee, Lee, & Hwang, 2006; Bamford et al., 2009; Deng et al., 2009; Kannappan, Guie, & Baker, 2009), and one could construct a red and blue bin with a divide at say $\mathfrak{M}_B = -18$ mag. Furthermore, a histogram would appear bimodal if one excluded the bridging population from the sample, but this would not be evidence against a single unified population but rather evidence of sample selection. Similarly, the observation (Figure 1) that ETGs fainter than $\mathfrak{M}_B = -18$ mag tend to have Sérsic indices $n < 2$ (exponential-like), while brighter ETGs tend to have $n > 2$ ($R^{1/4}$-like), is not evidence for two distinct populations. Similar caution is required for bulges.

7.2. $\mathfrak{M}$–μ_0

This section contains a summary of past efforts to provide a physical explanation for the artificial dichotomy at $\mathfrak{M}_B = -18$ mag. Of course, as seen above, there is no division of ETGs at $\mathfrak{M}_B = -18$ mag.

Some further historical context surrounding the $\mathfrak{M}$–μ_0 diagram should prove helpful and insightful.

While de Vaucouleurs' (1948, 1953, 1959) $R^{1/4}$ model for describing bright ETGs, and the bulges of disc galaxies, took hold, Hodge (1961*a*,b) had shown that de Vaucouleurs' model did not provide a good description of the faint ETGs. Hodge, Pyper, & Webb (1965) noted, in the concluding sentence of their article, that all of their dwarf ETGs displayed an exponential[af] light profile, as was shown in their Figures 4a–e. The influential article by Hodge (1971) also reported that the exponential model works well for the barred dwarf Im galaxy IC 1613, see also de Vaucouleurs (1961*a*) for other Irregular galaxies. This engendered suspicions of a connection between the discs at one end of the Aitken–Jeans–Lundmark–Hubble sequence and faint ETGs at the other. Faber & Lin (1983) and Binggeli et al. (1984) continued to show that the exponential model provides a reasonable description of the light profiles of faint ETGs. Kormendy (1985) subsequently added two generic disc galaxies from Freeman (1970) into his $\mathfrak{M}_B$–μ_0 diagram, to represent dwarf Irregular and late-type spiral galaxies near the bright-end of his skewed dwarf ETG distribution; see also K09 (their Figure 1) and Tolstoy et al. (2009, their Figure 1). Kormendy (1985) then went on to advocate that dwarf elliptical (dE) galaxies are better connected with the dwarf spiral and dwarf irregular galaxies found at the other end of the Aitken–Jeans–Lundmark–Hubble sequence and do not connect with ordinary ETGs at $\mathfrak{M}_B = -18$ mag. This view differed from Sandage & Binggeli (1984, see their Figure 1) who suggested a strong connection between dE and E galaxies, and a weak connection between dE and dwarf Irregular/Magellanic-like galaxies. In addition, Wirth & Gallagher (1984) had just suggested that compact elliptical (cE) galaxies (de Vaucouleurs, 1961*b*; Zwicky & Kowal, 1968; Zwicky & Zwicky, 1971) rather than dwarf ETGs may be the low-luminosity analogs of ordinary ETGs. Indeed, Fish (1963) had also noted that M32 defined the faint-end of his size–luminosity relation for elliptical galaxies, and K09 maintains this view.

With the availability of better spatially resolved data from the *HST*, Kormendy et al. (1994, see also Ferrarese et al., 1994 and Grillmair et al., 1994) used the $R^{1/4}$ model to describe the global properties of galaxies, and a double power-law model[ag] to describe their inner region. In order to measure the host galaxy light, they appropriately advocated for excluding the additional nuclear components (common in both dwarf and ordinary ETGs, and LTGs: e.g. Rest et al., 2001; Balcells et al., 2003; Böker et al., 2004), as can be seen in the light profiles shown by Lauer et al. (1995), Byun et al. (1996), and later K09. While the *HST* data revealed that it was galaxies with partially depleted cores that were deviating from the $\mathfrak{M}_B$–μ_0 relation defined by ordinary ETGs without cores — as previously reported by Oemler (1973) and Gudehus (1973) — Faber et al. (1997) claimed that if they had even better spatial resolution then they would obtain brighter central surface brightnesses for those ETGs without cores in the magnitude range $-18 > \mathfrak{M}_B > -20.5$ mag, thereby uniting the core-Sérsic and Sérsic galaxies with a linear relation in the $\mathfrak{M}$–μ_0 diagram and separating them from the dwarf ETGs. Faber et al. (1997, see their Figure 4) used the nearby, nucleated, Sérsic galaxy M32 as an example of this, including the nuclear star cluster in order to report the higher surface brightness required to make this galaxy follow the $\mathfrak{M}_B$–μ_0 relation defined by the luminous ETGs with depleted cores. This was, however, at odds with their treatment of other galaxies where they excluded additional nuclear components from the modelling process and obviously meant that they were no longer working with the properties of the host galaxy but were subject to the whims of nuclear star cluster formation.

Combining CCD images with deep, wide field-of-view, photographic data (Caon et al. (1993) and D'Onofrio et al. (1994)) had shown that the Sérsic function fits the brightness profiles of ETGs remarkably well over a large dynamic range. Graham & Guzmán (2003) and Balcells et al. (2003) used the Sérsic $R^{1/n}$ model to quantify HST-resolved galaxies and bulges. In addition, they *simultaneously* modelled the galaxy's discs and nuclear components, while Graham et al. (2003) showed how to unite the inner and outer regions of galaxies using the core-Sérsic model, rather than using a disconnected double power-law for the inner region and an $R^{1/4}$ model for the outer region. Furthermore, unlike the double power-law model, the Sérsic $R^{1/n}$ model previously applied to core-less galaxies has a finite central surface brightness, useful for quantifying the host bulge/galaxy μ_0 in galaxies without depleted cores, such as M32. Graham et al. (2003) and Balcells et al. (2003) advocated the identification and quantification of both central deficits (partially depleted cores) and excesses (additional nuclear components) relative to the inward extrapolation of the bulge's outer Sérsic profile, a practice later adopted by Ferrarese et al., 2006 and K09[ah]. Graham & Guzmán (2003) revealed that the $\mathfrak{M}_B$–μ_0 diagram displays no evidence for the alleged ETG divide at $\mathfrak{M}_B \approx -18$ mag that had been advocated by Kormendy (1985), Faber et al. (1997), and in numerous papers since then (e.g. Kormendy 2016, and references therein). Instead, Graham & Guzmán (2003) argued that the only magnitude of importance in this diagram is around $\mathfrak{M}_B = -20.5$ mag, corresponding to the division between ETGs whose spheroidal component had a Sérsic profile versus ETGs whose spheroidal component had a core-Sérsic profile. This magnitude corresponds to a mass of $(1-2) \times 10^{11}$ $M_\odot$.

[ae] As remarked in Graham & Soria (2019), this is not the case for stripped galaxies, whose stellar mass has been reduced but whose colour remains red.

[af] It is noted that an exponential (Sérsic $n = 1$) light profile can apply to both a three-dimensional ellipsoid and a two-dimensional disc.

[ag] See Hernquist (1990, his equation 43).

[ah] One point of distinction with K09 is that they consider 'Core' galaxies, that is, the core-Sérsic galaxies, to be slowly rotating, at odds with the known lenticular galaxies with depleted cores (e.g. Dullo & Graham, 2013, 2014).

https://doi.org/10.1017/pasa.2019.23 Published online by Cambridge University Press

7.3. Formation scenarios

It had become common to see papers refer to supernova-driven winds as the physical explanation for creating two disconnected species of ETG, with the winds blowing the gas out of the dwarf galaxies (e.g. Mathews & Baker, 1971; Saito, 1979) and making them different to ordinary ETGs. Dekel & Silk (1986) invoked supernova-driven winds for creating the two distinct classes of galaxies thought to have been observed in their $\mathfrak{M}_B$–$\langle\mu\rangle_e$ diagram. However, these studies over-looked the gravitational-binding energy of the dark matter halo (Mac Low & Ferrara, 1999)[ai]. A mechanism other than winds was therefore sought to explain the alleged discontinuity at $\mathfrak{M}_B \approx -18$ mag.

The claim that dwarf ETGs are formed from dIrrs had been challenged by Bothun et al. (1986; see also Hunter & Gallagher, 1985, their Figure 12), who reported that the irregular galaxies did not have the right magnitudes, surface brightnesses, nor colours, to evolve into dE galaxies. Investigating the structure of dwarf galaxies at near-infrared wavelengths, which are less affected by dust and the light from new stars, James (1991, 1994) similarly concluded that the dwarf Irr and dwarf ETGs differ markedly and it is unlikely that dwarf Irr galaxies transform into dwarf ETGs. Nonetheless, given the notion that ordinary elliptical galaxies formed from the merger of spiral galaxies (e.g. Toomre & Toomre, 1972), one can appreciate why the dwarf ETG population may have been suspected to have been morphologically transformed from something else. The absence of enough sufficiently low mass spiral galaxies (e.g. Sandage & Binggeli, 1984) that could merge and build the dwarf ETG population led to thoughts of yet alternative processes. Shapley (1951) had previously suggested that the Small Magellanic Cloud may be evolving into a dE galaxy, and Einasto et al. (1974), Frogel et al. (1982), Faber & Lin (1983), Lin & Faber (1983), Wirth & Gallagher (1984), and others similarly suggested that removing the gas content from a dwarf irregular galaxy may produce a dE galaxy; after all, they both had exponential light profiles.

Influenced by the shape of the light profile, there were speculations that the dwarf ETGs were associated with flat discs. However, the dEs were later shown to be ellipsoidal or at least not disc-like (e.g. Ichikawa et al., 1986). That is, an exponential-like (Sérsic $n = 1$) light profile does not necessarily imply a flat disc. Chen et al. (2010) wrote that 'The distribution of axial ratios of low-mass ('dwarf') galaxies bears a strong resemblance to the one observed for the higher-mass ('giant') galaxies'. Therefore, removing the gas from late-type spiral and Irregular galaxies, via the ram-pressure stripping from a galaxy cluster's hot X-ray gas, was not enough to explain the alleged (dwarf ETG) – (Irregular galaxy) connection. In passing, it is noted that ETGs can contain substantial discs, but as a population, they do not have the abundance of low bulge-to-total ratios as seen in late-type spiral and irregular galaxies.

Moore et al. (1996) subsequently revealed how multiple fast flybys past a massive perturbing galaxy, coupled with gravitational tidal forces within a galaxy cluster, could first invoke the formation of a bar within a small low-mass (Sd-like) disc galaxy and then strip away the remaining outer disc, leaving behind a somewhat harassed and puffed-up bar that was proposed to be the answer to the existence of dwarf ETGs and the lower-mass dSph galaxies in clusters. This mechanism maintained the suspected association with spiral galaxies and removed the connection with brighter ETGs. However, while the galaxy harassment scenario (Moore et al., 1996, 1998; Mastropietro et al., 2005, see also Mayer et al., 2001*a*,b) likely transforms low mass disc galaxies, it is unlikely to be capable of creating ETGs with $\mathfrak{M}_B = -16$ to -18 mag by stripping away much more luminous spiral galaxies. Moreover, a population of dynamically heated, but still rather flat, bars has not been observed in galaxy clusters. Instead, the dwarf ETGs are a population of multi-component galaxies possessing features that ordinary ($\mathfrak{M}_B \lesssim -18$ mag) ETGs, not thought to have been built by stripping/harassing of spiral galaxies, also contain. The existence of isolated dwarf ETGs, shown to have the same kinematic properties as dwarf ETGs in clusters (Janz et al., 2017; Graham et al., 2017), reveals that dwarf ETGs need not have been built by 'galaxy harassment'. They are thus built by Nature rather than Nurture: they do not require the harsh (nurturing) environment of a galaxy cluster to form.

The presence of disc-like features (e.g. Graham et al., 2003*b*; Lisker et al., 2006; Lisker & Fuchs, 2009) and rotation in dwarf ETGs in clusters — known since Davies et al. (1983) — had been heralded as evidence that they were previously spiral galaxies (e.g. Boselli et al., 2008; De Rijcke et al., 2010; Penny et al., 2014; Ryś et al., 2015; Toloba et al., 2015), even though ordinary ETGs display the very same features. Such discs, observed in ETGs up to $\sim 10^{11}$ $M_\odot$ (e.g. Emsellem et al. 2011; Krajnović et al. 2013), may be built from gas accretion and minor mergers (e.g. Schweizer, 1986; Schweizer & Seitzer, 1988; Birnboim & Dekel, 2003; Katz et al., 2003; Mei et al., 2006; Wei et al., 2010; Kaviraj et al., 2011). Structurally and kinematically, dwarf and ordinary ETGs (both in and out of clusters) display a continuum of disc-like features across the alleged divide at $\mathfrak{M}_B = -18$ mag.

As Tolstoy et al. (2009) note, in their Introduction's third paragraph, dwarf galaxies ($\mathfrak{M}_B > -16$ mag) form a continuum with brighter non-dwarf galaxies, in terms of potential well, size, structural, kinematic, and population features. Indeed, the dwarf and ordinary ETGs follow a continuous luminosity–metallicity relation (Dekel & Silk, 1986, see their Figure 2; Mateo 1998; Tremonti et al., 2004; Veilleux et al., 2005) which the Sm-Irr galaxies do not follow: the latter are less metal-rich than dwarf ETGs of the same luminosity (Mateo, 1998; Grebel, 2004). In addition, the L–σ relation reveals unity rather than division among the ETGs at $\mathfrak{M}_B = -18$ mag, with a continuous log-linear relation, having a slope of 2 in the B-band, which encompasses ETGs with $\mathfrak{M}_B \gtrsim -20.5$ mag (Davies et al., 1983; Matković & Guzmán, 2005; Hyde and Bernardi, 2009; Graham & Soria, 2019, see their Figure 1).

7.4. Bulges and discs

A large fraction of ETGs contain discs. Careful image analysis had previously revealed overlooked discs in many ETGs (e.g. Capaccioli, 1987), and subsequent kinematic studies revealed the prevalence of discs in ETGs (e.g. D'Onofrio et al., 1995; Graham et al., 1998; Pedraz et al., 2002; Emsellem et al. 2011; Scott et al., 2014). In addition, modern structural decompositions reveal multiple physical[aj] components in ETGs (e.g. Prieto et al., 2001; Läsker et al., 2014; Savorgnan & Graham, 2016; Sahu et al., 2019). Nowadays, in such studies, Sérsic's model provides an accurate description of the spheroidal component of the galaxy. In some

[ai] Of course today, AGN winds are invoked to blow away the gas in the ordinary ETGs, and both winds are expected to operate on a sliding-scale of efficiency unlikely to create two disjoint species of galaxy but rather a continuum.

[aj] I use the term 'physical component' to differentiate between blind decompositions involving multiple Sérsic components divorced from physically distinct entities.

https://doi.org/10.1017/pasa.2019.23 Published online by Cambridge University Press

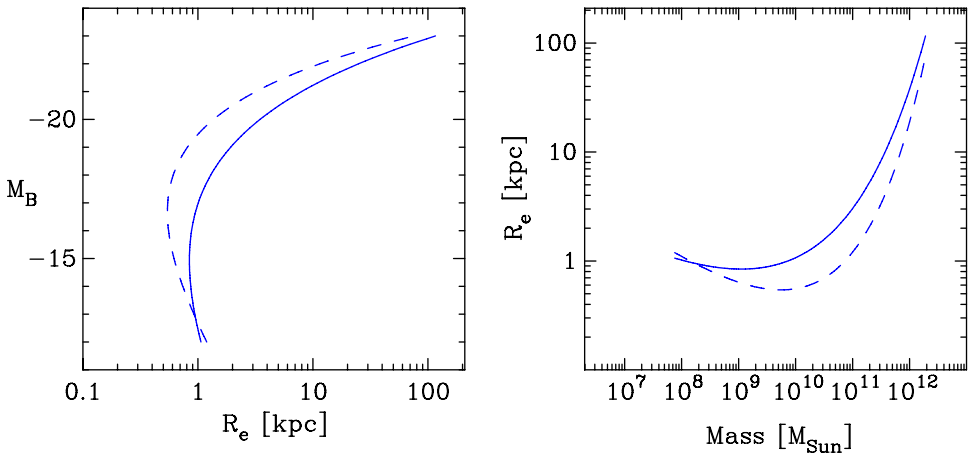

Figure 18. Left panel: The solid curve to the right is the $Z = 50\%$ curve from Figure 4, while the dashed curve to the left is the $Z = 50\%$ curve for bulges based upon equations 36 and 37. Right panel: Similar to the left-hand panel, but using simple mass estimates as explained in the text. While there is scope for improvement, one can see that bulges are naturally expected to be smaller than discy ETGs of the same mass. At high masses, the ETGs do not have discs, and the relationships converge. Perhaps the same is true at the low-mass end, although the upturn in bulge size seen here at low masses, and in Fisher & Drory (2016, see their Figure 1.4), is at odds with the bulge data in Figure 17 and Gadotti (2009).

instances, this is the entire galaxy, but ETGs less luminous than $\mathfrak{M}_B \approx -20.5$ mag invariably contain a disc, and sometimes a bar, ring, ansae, nuclear star cluster, or a more extended nuclear disc (e.g. de Vaucouleurs et al., 1991; Ferrarese et al., 2006; Saha et al. 2019). Not surprisingly, those studying galaxy structures have presented the $\mathfrak{M}$–log n and $\mathfrak{M}$–μ_0 relations for *bulges* and observed the offset from ETGs (e.g. Andredakis et al., 1995; Khosroshahi et al., 2000; Graham, 2001; Möllenhoff & Heidt, 2001; MacArthur et al., 2003).

7.4.1. Galaxy Bulges and Red Nuggets

For well over a decade, the galaxy size–luminosity relation, or rather, the R_e–(stellar mass, M_*) relation, has been used to argue that the compact ($R_e \lesssim 2$ kpc) massive ($M_* \gtrsim 10^{11}$ $M_\odot$) spheroidal-shaped galaxies at high-redshifts ($z \approx 2 \pm 1$) — referred to as 'red nuggets' by Damjanov et al. (2009) — must have evolved into large massive *elliptical* galaxies in the local ($z = 0$) Universe (e.g. Daddi et al., 2005; Kriek et al., 2006; Trujillo et al., 2006; van Dokkum, 2008). The argument has been that dry merger events have increased the size of the three-dimensional spheroidal structures, building elliptical galaxies rather than lenticular galaxies with large-scale discs. However, most ETGs in the local universe contain fast-rotating two-dimensional discs. In many instances, it is the disc which makes these galaxies large.

Graham et al., 2015 identified two dozen 'compact massive spheroids' as the bulge component of local lenticular galaxies. These bulges have the same distribution of sizes, masses, and Sérsic indices as the high-z compact massive galaxies and comparable number densities per unit volume of space (de la Rosa et al., 2016). This similarity strongly suggests that the above popular evolutionary scenario building bigger spheroids is not the complete picture. Rather, the evolution of these high-z red nuggets may instead be connected with the growth of discs (e.g. Caldwell, 1983*b*; Morganti et al., 2006; Sancisi et al., 2008; Stewart et al., 2009; Pichon et al., 2011; Moffett et al. 2012, 2015; Stark et al., 2013; Graham et al., 2015, see their Section 4.1; Kleiner et al., 2017). Gas accretion, both preceding and during 'cosmic noon', is expected to play a key role for the massive galaxies (Feldmann et al., 2016), while the less massive galaxies, that is, smaller over-densities, take longer to accrete smaller quantities of gas in a 'down-sizing' (Cowie et al., 1996) scenario (Graham et al., 2015, 2017).

It is insightful to compare the two key empirical relations for ETGs (equations 16 and 17) with the equivalent relations for the bulges of S0 galaxies and LTGs. Graham & Worley (2008) compiled K-band data for the bulges of ∼400 spiral and S0 galaxies, and Graham (2013) presented these two key equations for bulges (see his equations 2.19 and 2.20).[ak] They are such that

$$\mathfrak{M}_K = -7.5 \log(n) - 20.0 \text{ and} \quad (36)$$

$$\mathfrak{M}_K = 0.6\mu_{0,K} - 29.7. \quad (37)$$

We can take a quick look at how ETGs and bulges compare using the following rough transformation. Given the current interest in compact massive spheroids, a simple $B - K$ colour of 4 and a stellar mass-to-light ratio of 8 are used for everything. The left panel in Figure 18 shows the $\mathfrak{M}_B$–R_e relation for the ETGs (as seen in Figure 4) and the expected $\mathfrak{M}_B$–R_e relation for bulges (using equations 36 and 37, and assuming $B - K = 4$). Converting $\mathfrak{M}_B$ into a stellar mass using $\mathfrak{M}_{\odot,B} = 5.44$ mag (Mann & von Braun, 2015) and $M_*/L = 8$, the right-hand panel of Figure 18 displays the size–mass diagram using R_e. While varying stellar mass-to-light ratios are expected to alter the low-mass end, and it is not yet clear if the ETG bulge and the LTG bulge relations differ, one can see that bulges are in general more compact than ETGs (with discs) of the same mass. One can also see that at stellar masses above 2×10^{11} $M_\odot$, the bulge and ETG relations merge as the ETGs no longer have extended discs making them larger than their bulge component. This diagram supports the claim that some/many of the high-z compact massive galaxies are now the bulges of today's galaxies, having accreted and built a more substantial disc (Graham, 2013; Driver et al., 2013). Those stellar systems which only built an intermediate-scale disc, as opposed to a large-scale disc, are today's 'ellicular' (ES) galaxies (Liller, 1966; Graham et al., 2016, 2017).

[ak] Dust and colour gradients due to stellar population differences are expected to alter these equations from band to band. Kelvin et al. (2012) and Häußler et al. (2013) provide insight into this.

https://doi.org/10.1017/pasa.2019.23 Published online by Cambridge University Press

7.4.2. Pseudobulges

Balcells et al. (2003) were among the first to clearly call out lenticular and early-type spiral galaxies for not having bulges with $R^{1/4}$ light profiles. Laurikainen et al. (2006, 2005) and Graham & Worley (2008) further noted that most lenticular and spiral galaxies have near-infrared (K-band) bulge-to-total flux ratios less than one-third, thereby placing uncomfortable constraints on some simulations that were producing big $R^{1/4}$-like bulges (e.g. Abadi et al., 2003; Stewart et al., 2008). Weinzirl et al. (2009) also noted this absence of galaxies with big bulges having $R^{1/4}$-like profiles and high bulge-to-total flux ratios, and Kormendy et al. (2010) effectively took these trends to mean an abundance of pseudobulges built from the secular evolution of the discs. While some of these galaxies may have pseudobulges built from bars, one needs to be careful in identifying such bulges[al]. Moreover, many galaxies are alleged to contain both a pseudobulge and a classical bulge (e.g. Erwin et al., 2003; Peletier et al., 2007), making a mockery of attempts to divide galaxies based on whether they have a pseudobulge versus a classical bulge.

Parallel lines of thought on the bulges of disc galaxies and ETGs have contributed to the idea of pseudobulges having (exponential)-like light profiles and classical bulges built from different processes having ($R^{1/4}$)-like profiles (e.g. Carollo et al., 2001; Fisher & Drory, 2010, 2016, see their Figure 1.4), with some authors using a Sérsic index of 2 or 2.5 to divide bulges into one bin or the other. Graham & Worley (2008, see their Figure 8) showed that the S0, Sa, ...Sbc galaxy bulges (i.e. those with, in general, bright magnitudes and high Sérsic indices) roughly follow a linear μ_e–log R_e trend, while bulges in later type galaxies do not. This same pattern is evident in Fisher & Drory (2016, see their Figure 1.5, using data from Gadotti, 2009 and Fisher & Drory, 2010), who take this as evidence for a division between bulges. Gadotti (2009)[am] wrote 'We show that pseudobulges can be distinguished from classical bulges as outliers in the Kormendy relation', and 'our identification of pseudobulges [via this method] is not only more reliable but also better physically motivated.' This view was echoed by Blanton & Moustakas (2009) in their review of the physical properties of nearby galaxies. However, as we have seen, the μ_e–log R_e diagram is strongly curved with the value of both n and $\mathfrak{M}$ at the bend midpoint changing considerably depending on the arbitrary fraction of light used to define the effective radius. This above is, therefore, clearly not a signature of different formation physics occurring on either side of the bend midpoint.

Figure 5 reveals what the approximately linear log R_e–$\langle\mu\rangle_e$ relation is for bright ETGs, why it exists, and why it represents only a segment of a more encompassing, and unifying, curved distribution shown by the $Z = 50$ lines in Figure 5 and given by equations 2.14 and 2.15 in Graham (2013). Figure 5 also reveals why the lower-luminosity ETGs appear to deviate from the R_e–$\langle\mu\rangle_e$ relation, and why the scatter is larger at the low-luminosity end. It is a result of ETG structure systematically varying with absolute magnitude (a proxy for stellar mass). It is not an artefact of the Sérsic model: R_e and μ_e can be measured independently of the Sérsic model, and the curved trend remains (e.g. Trujillo et al., 2001; Figure 16). As revealed in 4.1, the absolute magnitude and Sérsic index corresponding to the bend midpoint are not a physically meaningful quantity that can be used to separate dwarf ETGs from ordinary ETGs, nor should it be used to divide pseudobulges from classical bulges. This becomes increasingly apparent when one realises that the bend midpoint occurs at a range of different magnitudes (and Sérsic indices) simply depending on what arbitrary fraction was used to measure the radii.

7.5. Fundamental planes

Bright ETGs, with Sérsic indices $n \gtrsim 3$, have similar light profiles over their inner 0.01–1.0 kpc, once excluding the presence of their depleted core or additional small-scale nuclear components such as nuclear discs, nuclear bars, AGN, or star clusters. One will therefore observe, from a sample of such bright ETGs with $n \gtrsim 3$, a clear relation between core radius and the associated surface brightness, even if there is no depleted core or if one dramatically over-estimates the core radius (so long as the estimate is $\lesssim$1 kpc). This was pointed out by Dullo & Graham (2012, see their Figure 18).

Among the ETGs with $n \gtrsim 3$, the ETGs with higher (lower) Sérsic indices, which are known to have higher (lower) stellar velocity dispersions (Graham, 2001), can be seen to have slightly higher (lower) surface densities in Figure 2. One can readily appreciate how folding in the stellar velocity dispersions with the (correct or incorrect) core radii and associated core surface brightnesses, to create a 'core fundamental plane' (Faber et al., 1997), will result in less lower scatter than that about the R_{core}–μ_{core} relation. This is because ETGs with $n \gtrsim 3$ that also have light profiles brighter (fainter) than the median light profile of ETGs with $n \gtrsim 3$ will have larger (smaller) velocity dispersions. How the slope of this 'core fundamental plane' might (not) be related to *dark matter* will be dealt with in a forthcoming paper, as will an investigation into the original 'Fundamental Plane' (Fish, 1963; Djorgovski and Davis, 1987).[an,ao] A related question regarding what radius is optimal for obtaining a tight plane, for both understanding ETGs and their use as a distance estimator for improved studies of peculiar velocity flows and cosmological parameter constraints (e.g. Johnson et al., 2014; da Cunha et al., 2017), will similarly be addressed, although some further insight is provided below.

Figure 5 reveals why the Fundamental Plane works; the reason is the same as why the 'core Fundamental Plane' (Faber et al., 1997) works. As noted above, for $\mathfrak{M}_B \lesssim -19$ mag, the ETG light profiles are such that they result in a bunching up of the μ_z–R_z and $\langle\mu\rangle_z$–R_z relations for different fractions z. At $\mathfrak{M}_B \lesssim -19$ mag, for a given mean surface brightness, the ETGs with brighter magnitudes — and thus higher Sérsic indices n, and also larger stellar velocity dispersions σ, plus redder colours and stronger metallicities (see de Vaucouleurs & Olson, 1982 and de Carvalho & Djorgovski, 1989) — will have larger scale radii. The introduction of such a third parameter (n or σ or colour or Mg_2 index) acts to counter this trend; and thus, the 'Fundamental Plane' has a reduced scatter than the μ_e–R_e and $\langle\mu\rangle_e$–R_e relations. Graham (2002*a*) introduced a 'Photometric Plane' in which n was used rather than σ or Mg_2.

Contradictory to the claims in Bender et al. (1992) and Burstein et al. (1997), the offset position of low-luminosity ETGs from the 'Fundamental Plane' defined by brighter ETGs (e.g. Kourkchi et al., 2012, see their Figure 9) is not a clear evidence that dwarf

[al] See Graham (2014, his Section 5) for a discussion of the difficulties with the assorted criteria used by some to identify pseudobulges.

[am] The Gadotti (2009) data are not quite as expected, in that their bulges do not display a slight upturn in size at masses below $\sim 3 \times 10^9$ $M_\odot$ or $n \lesssim 2$ (cf. Fisher & Drory, 2016, see their Figure 1.5).

[an] Fish (1963) reported that, if homology holds, then $(L/R_e)^{1/2} \propto \sigma$ or $R_e \propto \sigma^2 \langle I\rangle_e^{-1}$.

[ao] Djorgovski and Davis, 1987, also assuming $R^{1/4}$-model homology, reported $R_e \propto \sigma^{1.39} \langle I\rangle_e^{-0.90}$.

https://doi.org/10.1017/pasa.2019.23 Published online by Cambridge University Press

galaxies are a different species of galaxy to ordinary ETGs with a divide occurring at $\mathfrak{M}_B \approx -18$ mag. The proof is simple: use of radii and mean surface brightnesses, enclosing a different percentage of the galaxy light, will result in a different mass range of ETGs appearing included or offset from the revised plane defined by the brighter galaxies.

More recently, a division between bulges with $n \approx 4$ and $n \approx 1$ has been carried over into research into massive black holes, with several authors referring to low mass bulges as pseudobulges (e.g. Kormendy & Ho, 2013; Ho & Kim, 2014; Heckman & Best, 2014; Somerville & Davé, 2015). As Davis et al. (2018) point out, almost every spiral galaxy with a directly measured black hole mass has been alleged to contain a pseudobulge. A warning is therefore issued here for studies searching for a plane within three-dimensional spaces involving black hole mass and bulge (or galaxy) effective radii (e.g. Marconi & Hunt, 2003; de Francesco et al., 2006; Barway & Kembhavi, 2007; Saglia et al., 2016; van den Bosch, 2016). The use of half-light parameters is going to result in a curved manifold rather than a plane, and the slopes of reported planes will be a function of one's sample selection boundary. Departures at low black hole masses, from the plane constructed by galaxies with high black hole masses, need not be a sign of different formation physics. This should be independent of the (R_e-independent)-observation that the bulges of LTGs follow a different M_{bh}–(bulge luminosity) relation than the bulges of ETGs (Savorgnan et al., 2016; Davis et al., 2018, 2019; Sahu et al., 2019).

8. Conclusions

In the late 1980s, a growing body of increasingly accurate photometry revealed that the $R^{1/4}$ model was not a universal law for bright ETGs, and nor was the exponential model universal for faint ETGs (see Capaccioli 1985, 1987, 1989; Schombert, 1986; Davies et al., 1988). Subsequent analyses revealed that Sérsic's $R^{1/n}$ model both provided a superior description of the galaxy light and unified the faint and bright ETGs (e.g. Caon et al., 1993). This not only eliminated the prime reason ($R^{1/4}$ model versus exponential ellipsoid model) that had led to thoughts and theories dividing faint and bright ETGs, but it also provided the necessary clue for understanding the (curved) distributions in the 'effective' parameter scaling diagrams. However, this revolution ($R^{1/n}$ model) came too late, experienced 10–15 years of considerable opposition due to perceptions that the $R^{1/4}$ model was some kind of physical law of nature, and its implications are yet to permeate much of the field. Nonetheless, it should be noted that in the early 1980s, Binggeli, Bothun, Caldwell, Sandage, and their collaborators, were correct in their understanding of the continuum between dwarf and normal ETGs, as understood by Gudehus and Oemler a decade before that.

R_e, or not R_e? Perhaps that should be the question. Given the nature of ETG light profiles, those using R_e, or μ_e or $\langle\mu\rangle_e$, need to have an awareness of what these quantities are, beyond the obvious superficial meaning related to the radius containing 50% of the galaxies' light. Studies attaching a physical meaning to slopes or bends in diagrams using these 'effective parameters' need to be carefully considered given that a radius containing a different percentage of the galaxies' light will yield different (equally physically-meaningless) slopes and bend-points.

Acknowledgements. While Graham & Guzmán (2003) and Graham (2013) used the surface brightness at and within R_e to indirectly reveal the issue with R_e, I thank the Australian Research Council's funding scheme DP17012923 which enabled me the opportunity to more directly and fully explain here why R_e has been such a misleading quantity. I am additionally indebted to the Swinburne Research Sabbatical Scheme.

References

Abadi, M. G., Navarro, J. F., Steinmetz, M., & Eke, V. R. 2003, ApJ, 591, 499
Aitken, R. G. 1906, PASP, 18, 111
Andredakis, Y. C., Peletier, R. F., & Balcells, M. 1995, MNRAS, 275, 874
Anglés-Alcázar, D., Davé, R., Faucher-Giguère, C.-A., Özel, F., & Hopkins, P. F. 2017, MNRAS, 464, 2840
Balcells, M., Graham, A. W., Domínguez-Palmero, L., & Peletier, R. F. 2003, ApJL, 582, L79
Balcells, M., Graham, A. W., & Peletier, R. F. 2007, ApJ, 665, 1104
Bamford, S. P., Nichol, R. C., Baldry, I. K., et al. 2009, MNRAS, 393, 1324
Barai, P., Viel, M., Murante, G., Gaspari, M., & Borgani, S. 2014, MNRAS, 437, 1456
Barway, S., & Kembhavi, A. 2007, ApJL, 662, L67
Baum, W. A. 1959, PASP, 71, 106
Begelman, M. C., Blandford, R. D., Rees, M. J. 1980, Nature, 287, 307
Bekki, K., Couch, W. J., Drinkwater, M. J., & Gregg, M. D. 2001, ApJL, 557, L39
Bender, R., Burstein, D., & Faber, S. M. 1992, ApJ, 399, 462
Bender, R., Kormendy, J., Cornell, M. E., & Fisher, D. B. 2015, ApJ, 807, 56
Benson, A. J. 2012, Nature, 17, 175
Bershady, M. A., Jangren, A., & Conselice, C.J. 2000, AJ, 119, 2645
Bigay, J. H., & Paturel, G. 1980, A&A Supp., 42, 69
Bildfell, C., Hoekstra, H., Babul, A., & Mahdavi, A. 2008, MNRAS, 389, 1637
Binggeli, B., 1985, in Star-Forming Dwarf Galaxies and Related Objects, ed. D. Kunth, T. X. Thuan, J. T. T. Van, p.53, Gif sur Yvette, Fr: Ed. Front
Binggeli, B., Cameron, L. M. 1991, A&A, 252, 27
Binggeli, B., Jerjen, H. 1998, A&A, 333, 17
Binggeli, B., Sandage, A., & Tammann, G. A. 1985, AJ, 90, 1681
Binggeli, B., Sandage, A., Tarenghi, M. 1984, AJ, 89, 64
Binney, J., & Tremaine, S. 1987, Princeton, NJ, Princeton University Press
Birnboim, Y., & Dekel, A. 2003, MNRAS, 345, 349
Blanton, M. R., Dalcanton, J., Eisenstein, D., et al. 2001, AJ, 121, 2358
Blanton, M. R., & Moustakas, J. 2009, ARA&A, 47, 159
Böker, T., Sarzi, M., McLaughlin, D. E., et al. 2004, AJ, 127, 105
Bonfini, P., González-Martín, O., Fritz, J., et al. 2018, MNRAS, 478, 1161
Boselli, A., Boissier, S., Cortese, L., & Gavazzi, G. 2008, ApJ, 674, 742
Bothun, G. D., Mould, J. R., Caldwell, N., & MacGillivray, H. T. 1986, AJ, 92, 1007
Bower, R. G., Benson, A. J., Malbon, R., et al. 2006, MNRAS, 370, 645
Brookes, R. A., Rood, H. J. 1971, Astrophysical Letters, 8, 61
Bryan, G. L., & Norman, M. L. 1998, ApJ, 495, 80 H. 2008. Ap. J. Lett. 687:L61–64
Burstein, D., Bender, R., Faber, S., & Nolthenius, R. 1997, AJ, 114, 1365
Burstein, D., Davies, R. L., Dressler, A., et al. 1987, ApJS, 64, 601
Byun, Y.-I., Grillmair, C. J., Faber, S. M., et al. 1996, AJ, 111, 1889
Caldwell, N. 1983, AJ, 88, 804
Caldwell, N. 1983, ApJ, 268, 90
Caldwell, N., & Bothun, G. D. 1987, AJ, 94, 1126
Campbell, D. J. R., Frenk, C. S., Jenkins, A., et al. 2017, MNRAS, 469, 2335
Cappellari, M. 2016, ARA&A 54, 597
Cappellari, M., Bacon, R., Bureau, M., et al. 2006, MNRAS, 366, 1126
Cappellari, M., Scott, N., Alatalo, K., et al. 2013a, MNRAS, 432, 1709
Cappellari, M., McDermid, R. M., Alatalo, K., et al. 2013b, MNRAS, 432, 1862
Caon, N., Capaccioli, M., D'Onofrio, M. 1993, MNRAS, 265, 1013
Caon, N., Capaccioli, M., D'Onofrio, M. 1994, A&AS, 106, 199
Caon, N., Capaccioli, M., Rampazzo, R. 1990, A&AS, 86, 429
Capaccioli, M. 1985, in New Aspects of Galaxy Photometry, ed. J.-L. Nieto (Springer-Verlag), 53
Capaccioli, M. 1987, in Structure and Dynamics of Elliptical Galaxies, IAU Symp. 127 (Reidel, Dordrecht), 47
Capaccioli, M. 1989, in The World of Galaxies, ed. H. G. Corwin, L. Bottinelli (Berlin: Springer-Verlag), 208
Capaccioli, M., Caon, N. 1991, MNRAS, 248, 523

https://doi.org/10.1017/pasa.2019.23 Published online by Cambridge University Press

Capaccioli, M., Caon, N., & D'Onofrio, M. 1994, Memorie della Società Astronomia Italiana, 65, 919
Carlberg, R. G., Yee, H. K. C., & Ellingson, E. 1997, ApJ, 478, 462
Carollo, C. M., Stiavelli, M., de Zeeuw, P. T., Seigar, M., & Dejonghe, H. 2001, ApJ, 546, 216
Cellone, S. A., Forte, J. C., Geisler, D. 1994, ApJS, 93, 397
Chen, C.-W., Côté, P., West, A. A., Peng, E. W., & Ferrarese, L. 2010, ApJS, 191, 1
Chilingarian, I., Cayatte, V., Revaz, Y., et al. 2009, Science, 326, 1379
Chilingarian, I., & Zolotukhin, I. 2015, Science, 348, 418
Clausius, R. J. E. 1870, Annalen der Physik, vol. 217, Issue 9, p.124 (translated: Philosophical Magazine, Series 4., v. 40, p.122)
Ciotti L. 1991, A&A, 249, 99
Côté, P., Blakeslee, J. P., Ferrarese, L., et al. 2004, ApJS, 153, 223
Côté, P., Ferrarese, L., Jordán, A., et al. 2007, ApJ, 671, 1456
Côté, P., Piatek, S., Ferrarese, L., et al. 2006, ApJS, 165, 57
Courteau, S., de Jong, R. S., & Broeils, A. H. 1996, ApJL, 457, L73
Cowie, L. L., Songaila, A., Hu, E. M., & Cohen, J. G. 1996, AJ, 112, 839
Croton, D. J., Springel, V., White, S. D. M., et al. 2006, MNRAS, 365, 11
da Cunha, E., Hopkins, A. M., Colless, M., et al. 2017, PASA, 34, e047
Daddi E. Renzini A., Pirzkal N., Cimatti A., Malhotra S., et al. 2005, ApJ, 626, 680
Damjanov I, McCarthy PJ, Abraham RG, Glazebrook K, Yan H, et al. 2009, ApJ, 695, 101
Davies, J. I., Phillipps, S., Cawson, M. G. M., Disney, M. J., Kibblewhite, E. J. 1988, MNRAS, 232, 239
Davies, R. L., Efstathiou, G., Fall, S. M., Illingworth, G., & Schechter, P. L. 1983, ApJ, 266, 41
Davis, B. L., Graham, A. W., & Cameron, E. 2018, ApJ, 869, 113
Davis, B. L., Graham, A. W., & Cameron, E. 2019, ApJ, in press, arXiv:1810.04887
de Carvalho, R. R., & Djorgovski, S. 1989, ApJL, 341, L37
de Francesco, G., Capetti, A., & Marconi, A. 2006, A&A, 460, 439
Dekel, A., & Silk, J. 1986, ApJ, 303, 39
de la Rosa, I. G., La Barbera, F., Ferreras, I., et al. 2016, MNRAS, 457, 1916
Deng, X.-F., He, J.-Z., Wu, P., & Ding, Y.-P. 2009, ApJ, 699, 948
De Rijcke, S., Van Hese, E., & Buyle, P. 2010, ApJL, 724, L171
de Vaucouleurs, G. 1948, Annales d'Astrophysique, 11, 247
de Vaucouleurs, G. 1953, MNRAS, 113, 134
de Vaucouleurs, G. 1959, in Handbuch der Physik, ed. S. Flügge (Berlin: Springer), 311
de Vaucouleurs, G. 1961a, Astrophys. J. 133, 405
de Vaucouleurs, G. 1961b, ApJS, 5, 233 ApJS, 33, 211
de Vaucouleurs, G. 1977, in Evolution of Galaxies and Stellar Populations, Proceedings of a Conference at Yale University, May 19–21, 1977, ed. B. M. Tinsley & R. B. Larson (New Haven: Yale University Observatory), 43
de Vaucouleurs, G., Capaccioli, M. 1979, ApJS, 40, 669
de Vaucouleurs, G., de Vaucouleurs, A., Corwin, H. G., Jr., Buta, R. J.; Paturel, G.; Fouqué, P. 1991, Third Reference Catalogue of Bright Galaxies (New York: Springer)
de Vaucouleurs, G., & Olson, D. W. 1982, ApJ, 256, 346
de Vaucouleurs, G., & Page, J. 1962, ApJ, 136, 107
Djorgovski, S., Davis M. 1987, ApJ, 313, 59
D'Onofrio, M., Capaccioli, M., Caon, N. 1994, MNRAS, 271, 523
D'Onofrio, M., Zaggia, S. R., Longo, G., Caon, N., & Capaccioli, M. 1995, A&A, 296, 319
Driver, S. P., Allen, P. D., Graham, A. W., et al. 2006, MNRAS, 368, 414
Driver, S. P., Robotham, A. S. G., Bland-Hawthorn, J., et al. 2013, MNRAS, 430, 2622
Drory, N., Bender, R., & Hopp, U. 2004, ApJL, 616, L103
Dullo, B. T., & Graham, A. W. 2012, ApJ, 755, 163
Dullo, B. T., & Graham, A. W. 2013, ApJ, 768, 36
Dullo, B. T., & Graham, A. W. 2014, MNRAS, 444, 2700
Einasto, J., Saar, E., Kaasik, A., & Chernin, A. D. 1974, Nature, 252, 111
Emsellem, E., Cappellari, M., Krajnović, D., et al. 2011, MNRAS, 414, 888
Erwin, P., Beltrán, J. C. V., Graham, A. W., & Beckman, J. E. 2003, ApJ, 597, 929
Faber, S. M., Lin, D. M. C. 1983, ApJ, 266, L17
Faber, S. M., Tremaine, S., Ajhar, E. A., et al. 1997, AJ, 114, 1771
Famaey, B., & McGaugh, S. S. 2012, Living Reviews in Relativity, 15, 10
Farouki, R. T., Shapiro, S. L., & Duncan, M. J. 1983, ApJL, 265, 597
Feldmann, R., Hopkins, P. F., Quataert, E., Faucher-Giguère, C.-A., & Kereš, D. 2016, MNRAS, 458, L14
Ferrarese, L., Côté, P., Jordán, A., et al. 2006, ApJS, 164, 334
Ferrarese, L., Côté, P., Sánchez-Janssen, R., et al. 2016, ApJ, 824, 10
Ferrarese, L., van den Bosch, F. C., Ford, H. C., Jaffe, W., & O'Connell, R. W. 1994, AJ, 108, 1598
Fish, R. A. 1963, AJ, 68, 72
Fish, R. A. 1964, ApJ, 139, 284
Fisher, D. B., Drory, N. 2010, ApJ, 716, 942
Fisher, D. B., & Drory, N. 2016, in Laurikainen E., Peletier R. F., Gadotti D., eds, Galactic Bulges, Astrophysics and Space Science Library, Vol. 418 (Cham: Springer International Publishing Switzerland), 41
Forbes, D. A., Lasky, P., Graham, A. W., & Spitler, L. 2008, MNRAS, 389, 1924
Forbes, D. A., Spitler, L. R., Graham, A. W., et al. 2011, MNRAS, 413, 2665
Fraser, C. W. 1977, A&A Supp. Ser., 29, 161
Freeman, K. C. 1970, ApJ, 160, 811
Frogel, J. A., Blanco, V. M., McCarthy, M. F., & Cohen, J. G. 1982, ApJ, 252, 133
Fraser, C. W. 1972, The Observatory, 92, 51
Gabor, J. M., & Bournaud, F. 2014, MNRAS, 441, 1615
Gadotti, D. A. 2009, MNRAS, 393, 1531
Gavazzi, G., Donati, A., Cucciati, O., et al. 2005, A&A, 430, 411
Genel, S., Vogelsberger, M., Springel, V., et al. 2014, MNRAS, 445, 175
Graham, A. W. 2001, AJ, 121, 820
Graham, A. W. 2002a, MNRAS, 334, 859
Graham, A. W. 2002b, ApJL, 568, L13
Graham, A. W. 2005, in IAU Coll. 198, Near-fields Cosmology with Dwarf Elliptical Galaxies, ed. H. Jerjen & B. Binggeli (Cambridge: Cambridge University Press), 303
Graham, A. W. 2013, in Planets, Stars and Stellar Systems, 6, 91–140, ed. T. D. Oswalt & W. C. Keel (Springer Publishing) (arXiv:1108.0997)
Graham, A. W. 2014, in Structure and Dynamics of Disk Galaxies. Proceedings of the Conference held 12-16 August, 2013 at the Winthrop Rockefeller Institute, Petit Jean Mountain, Arkansas, USA. ed. M.S. Seigar & P. Treuthardt. ASP Conference Series (Vol. 480), 185
Graham, A. W. 2019, MNRAS, 487, 4995
Graham, A. W. Mck. 2016, in 'From the Realm of the Nebulae to Populations of Galaxies: Dialogues on a century of Research, ed. M. D'Onofrio, R. Rampazzo, & S. Zaggia (Vol. 435; Springer International Publishing Switzerland, Astrophysics and Space Science Library), 338
Graham, A. W., Ciambur, B. C., & Savorgnan, G. A. D. 2016, ApJ, 831, 132
Graham, A., & Colless, M. 1997, MNRAS, 287, 221
Graham, A. W., Colless, M. M., Busarello, G., Zaggia, S., & Longo, G. 1998, A&A Supp., 133, 325
Graham, A. W., Dullo, B. T., & Savorgnan, G. A. D. 2015, ApJ, 804, 32
Graham, A. W., & Driver, S. P. 2005, PASA, 22, 118
Graham, A. W., Erwin, P., Trujillo, I., & Asensio Ramos, A. 2003, AJ, 125, 2951
Graham, A. W., & Guzmán, R. 2003, AJ, 125, 2936
Graham, A. W., & Guzman, R. 2004, in Penetrating Bars Through Masks of Cosmic Dust, ed. D. L. Block et al., (Vol. 319; Dordrecht: Kluwer), 723
Graham, A. W., Janz, J., Penny, S. J., et al. 2017, ApJ, 840, 68
Graham, A. W., Jerjen, H., & Guzmán, R. 2003b, AJ, 126, 1787
Graham, A., Lauer, T. R., Colless, M., & Postman, M. 1996, ApJ, 465, 534
Graham, A. W., Merritt, D., Moore, B., Diemand, J., & Terzić, B. 2006, AJ, 132, 2711
Graham, A. W., & Soria, R. 2019, MNRAS, 484, 794
Graham, A. W., Trujillo, I., & Caon, N. 2001, AJ, 122, 1707
Graham, A. W., & Worley, C. C. 2008, MNRAS, 388, 1708
Graves, G. J., & Faber, S. M. 2010, ApJ, 717, 803
Graham, A. W. 2019, MNRAS
Grebel, E. K. 2004, in Carnegie Observatories Astrophysics Series 4, Origin and Evolution of the Elements, ed. A. McWilliam & M. Rauch (Cambridge: Cambridge University Press), 234
Grillmair, C. J., Faber, S. M., Lauer, T. R., et al. 1994, AJ, 108, 102
Gudehus, D. H. 1973, AJ, 78, 583

https://doi.org/10.1017/pasa.2019.23 Published online by Cambridge University Press

Gudehus, D. H., & Hegyi, D. J. 1991, AJ, 101, 18
Häußler, B., Bamford, S. P., Vika, M., et al. 2013, MNRAS, 430, 330
Heckman, T. M., & Best, P. N. 2014, ARA&A, 52, 589
Heidmann, J. 1967, C. R. Acad. Sci., 265 B, 866
Heidmann, J. 1969, Astrophys. Lett., 3, 19
Helmi, A., Babusiaux, C., Koppelman, H. H., et al. 2018, Nature, 563, 85
Hernquist, L. 1990, ApJ, 356, 359
Hilker, M., Mieske, S., & Infante, L. 2003, A&A, 397, L9
Hills, J. G. 1988, Nature, 331, 687
Ho, L. C., & Kim, M. 2014, ApJ, 789, 17
Hodge, P. W. 1961a, AJ, 66, 249
Hodge, P. W. 1961b, AJ, 66, 384
Hodge, P. W. 1971, ARA&A, 9, 35
Hodge, P. W., Pyper, D. M., & Webb, C. J. 1965, AJ, 70, 559
Holmberg, E. 1969, Arkiv for Astronomi, 5, 305
Huang, K.-H., Fall, S. M., Ferguson, H. C., et al. 2017, ApJ, 838, 6
Hubble, E. P. 1926, ApJ, 64, 321
Hubble, E. 1930, ApJ, 71, 231
Hubble, E. P. 1936, Realm of the Nebulae, by E.P. Hubble, New Haven: Yale University Press
Hunter, D. A., & Gallagher, J. S., III 1985, ApJS, 58, 533
Hyde, J.B., Bernardi, M. 2009. Mon. Not. R. Astron. Soc. 394, 1978–90
Ichikawa, S.-I., Wakamatsu, K.-I., & Okamura, S. 1986, ApJS, 60, 475
James, P. 1991, MNRAS, 250, 544
James, P. A. 1994, MNRAS, 269, 176
Janz, J., Penny, S. J., Graham, A. W., Forbes, D. A., & Davies, R. L. 2017, MNRAS, 468, 2850
Jeans J. 1919. Problems of Cosmogony and Stellar Dynamics (Cambridge: Cambridge University Press)
Jeans, J. H. 1928, Astronomy & Cosmogony (Cambridge: Cambridge University Press), 332
Jerjen, H., Binggeli, B. 1997, in The Nature of Elliptical Galaxies; The Second Stromlo Symposium, ASP Conf. Ser., 116, 239
Jerjen, H., Binggeli, B., & Freeman, K. C. 2000, AJ, 119, 593
Johnson, A., Blake, C., Koda, J., et al. 2014, MNRAS, 444, 3926
Kannappan, S. J., Guie, J. M., & Baker, A. J. 2009, AJ, 138, 579
Katz, N., Keres, D., Dave, R., & Weinberg, D. H. 2003, The IGM/Galaxy Connection. The Distribution of Baryons at z=0, 281, 185
Kaviraj, S., Tan, K.-M., Ellis, R. S., & Silk, J. 2011, MNRAS, 411, 2148
Kelvin, L. S., Driver, S. P., Robotham, A. S. G., et al. 2012, MNRAS, 421, 1007
Kennedy, R., Bamford, S. P., Häußler, B., et al. 2016a, A&A, 593, A84
Kennedy, R., Bamford, S. P., Häußler, B., et al. 2016b, MNRAS, 460, 3458
Kent, S. M. 1985, ApJS, 59, 115
Kent, S. M. 1990, Evolution of the Universe of Galaxies, 10, 109
Khosroshahi, H. G., Wadadekar, Y., & Kembhavi, A. 2000, ApJ, 533, 162
King, I. 1962, AJ, 67, 471
King, I. R. 1966, AJ, 71, 64
King, I. R. 1978, ApJ, 222, 1
King I.R., Minkowski R. 1966, ApJ, 143, 1002
King I.R., Minkowski R. 1972, IAU Symp., 44, 87
Kleiner, D., Pimbblet, K. A., Jones, D. H., Koribalski, B. S., & Serra, P. 2017, MNRAS, 466, 4692
Kodaira, K., Okamura, S., & Watanabe, M. 1983, ApJL, 274, L49
Kormendy, J. 1977, ApJ, 218, 333
Kormendy, J. 1985, ApJ, 295, 73
Kormendy, J. 2016, in Galactic Bulges', Astrophysics and Space Science Library, ed. E. Laurikainen, R. F. Peletier, D. Gadotti (Vol. 418; Cham: Springer International Publishing Switzerland), 431
Kormendy, J., & Bender, R. 2012, ApJS, 198, 2
Kormendy, J., & Djorgovski, S. 1989, ARA&A, 27, 235
Kormendy, J., Drory, N., Bender, R., & Cornell, M. E. 2010, ApJ, 723, 54
Kormendy, J., Dressler, A., Byun, Y. I., et al. 1994, European Southern Observatory Conference and Workshop Proceedings, 49, 147
Kormendy, J., Fisher, D. B., Cornell, M. E., Bender, R. 2009, ApJS, 182, 216
Kormendy, J., & Ho, L. C. 2013, ARA&A, 51, 511
Kourkchi, E., Khosroshahi, H. G., Carter, D., & Mobasher, B. 2012, MNRAS, 420, 2835
Krajnović, D., Alatalo, K., Blitz, L., et al. 2013, MNRAS, 432, 1768
Kravtsov, A. V. 2013, ApJL, 764, L31
Kriek, M., van Dokkum, P. G., Franx, M., et al. 2006, ApJL, 649, L71
Kroupa, P., Famaey, B., de Boer, K. S., et al. 2010, A&A, 523, A32
Lange, R., Driver, S. P., Robotham, A. S. G., et al. 2015, MNRAS, 447, 2603
Läsker, R., Ferrarese, L., & van de Ven, G. 2014, ApJ, 780, 69
Lauer, T. R., Ajhar, E. A., Byun, Y.-I., et al. 1995, AJ, 110, 2622
Laurikainen, E., Salo, H., Buta, R., et al. 2006, AJ, 132, 2634
Laurikainen, E., Salo, H., & Buta, R. 2005, MNRAS, 362, 1319
Lee, J. H., Lee, M. G., & Hwang, H. S. 2006, ApJ, 650, 148
Liller, M. H. 1966, ApJ, 146, 28
Lin, D. N. C., & Faber, S. M. 1983, ApJL, 266, L21
Lisker, T., & Fuchs, B. 2009, A&A, 501, 429
Lisker, T., Grebel, E. K., & Binggeli, B. 2006, AJ, 132, 497
Lundmark, K. 1925, MNRAS, 85, 865
Lundmark, K. 1927, Nova Acta Regiae Soc. Sci. Upsaliensis, Volumen Extra Ordinem Editum, 1
Lyskova, N., Thomas, J., Churazov, E., Tremaine, S., & Naab, T. 2015, MNRAS, 450, 3442
MacArthur, L. A., Courteau, S., & Holtzman, J. A. 2003, ApJ, 582, 689
Macciò, A. V., Murante, G., & Bonometto, S. P. 2003, ApJ, 588, 35
Mac Low, M.-M., & Ferrara, A. 1999, ApJ, 513, 142
Mann, A. W., & von Braun, K. 2015, PASP, 127, 102
Marconi, A., & Hunt, L. K. 2003, ApJL, 589, L21
Mastropietro, C., Moore, B., Mayer, L., et al. 2005, MNRAS, 364, 607
Mateo, M. L. 1998, ARA&A, 36, 435
Mathews, W. G., & Baker, J. C. 1971, ApJ, 170, 241
Matković, A., & Guzmán, R. 2005, MNRAS, 362, 289
Mayer, L., Governato, F., Colpi, M., et al. 2001a, ApJ, 559, 754
Mayer, L., Governato, F., Colpi, M., et al. 2001b, ApJL, 547, L123
Mei, S., Blakeslee, J. P., Côté, P., et al. 2007, ApJ, 655, 144
Mei, S., Blakeslee, J. P., Stanford, S. A., et al. 2006, ApJ, 639, 81
Michard, R. 1979, A&A, 74, 206
Misgeld, I., Mieske, S., & Hilker, M. 2008, A&A, 486, 697
Misgeld, I., Hilker, M., & Mieske, S. 2009, A&A, 496, 683
Misgeld, I., & Hilker, M. 2011, MNRAS, 414, 3699
Milgrom, M. 1983, ApJ, 270, 365
Milgrom, M., & Sanders, R. H. 2003, ApJL, 599, L25
Moffett, A. J., Kannappan, S. J., Baker, A. J., & Laine, S. 2012, ApJ, 745, 34
Moffett, A. J., Kannappan, S. J., Berlind, A. A., et al. 2015, ApJ, 812, 89
Möllenhoff, C., & Heidt, J. 2001, A&A, 368, 16
Moore, B., Katz, N., Lake, G., Dressler, A., & Oemler, A. 1996, Nature, 379, 613
Moore, B., Lake, G., & Katz, N. 1998, ApJ, 495, 139
Morgan, W. W. 1958, PASP, 70, 364
Morgan, W. W. 1959, PASP, 71, 394
Morgan, W. W. 1962, ApJ, 135, 1
Morgan, W. W., & Mayall, N. U. 1957, PASP, 69, 291
Morganti, R., de Zeeuw, P. T., Oosterloo, T. A., et al. 2006, MNRAS, 371, 157
Muñoz-Mateos, J. C., Sheth, K., Regan, M., et al. 2015, ApJS, 219, 3
Mutlu-Pakdil, B., Seigar, M. S., Hewitt, I. B., et al. 2018, MNRAS, 474, 2594
Naab, T., Johansson, P. H., Ostriker, J. P. 2009. Ap. J. Lett. 699:L178–82
Nair, P., van den Bergh, S., & Abraham, R. G. 2011, ApJL, 734, L31
Oemler, A. 1973, ApJ, 180,
Oemler, A., Jr. 1976, ApJ, 209, 693
Patterson, F. S., 1940, Harvard College Observatory Bulletin, 914, 9
Pedraz, S., Gorgas, J., Cardiel, N., Sánchez-Blázquez, P., & Guzmán, R. 2002, MNRAS, 332, L59
Peletier, R. F., Falcón-Barroso, J., Bacon, R., et al. 2007, MNRAS, 379, 445
Penny, S. J., Conselice, C. J. 2008, MNRAS, 383, 247
Penny, S. J., Forbes, D. A., Pimbblet, K. A., & Floyd, D. J. E. 2014, MNRAS, 443, 3381
Petrosian, V. 1976, ApJL, 209, L1
Pichon, C., Pogosyan, D., Kimm, T., et al. 2011, MNRAS, 418, 2493
Planck Collaboration, Ade, P. A. R., Aghanim, N., et al. 2016, A&A, 594, A13
Poincare, H., & Vergne, H. 1911, Paris, A. Hermann et fils, 1911.,
Poveda, A. 1958, Boletin de los Observatorios Tonantzintla y Tacubaya, 2, 3
Poveda, A. 1961, ApJ, 134, 910

https://doi.org/10.1017/pasa.2019.23 Published online by Cambridge University Press

Prieto, M., Aguerri, J. A. L., Varela, A. M., & Muñoz-Tuñón, C. 2001, A&A, 367, 405
Prugniel, P., & Simien, F. 1997, A&A, 321, 111
Ragone-Figueroa, C., Granato, G. L., Murante, G., Borgani, S., & Cui, W. 2013, MNRAS, 436, 1750
Remus, R.-S., Dolag, K., Bachmann, L. K., et al. 2015, Galaxies in 3D across the Universe, 309, 145
Rest, A., van den Bosch, F. C., Jaffe, W., et al. 2001, AJ, 121, 2431
Reynolds, J. H. 1913, MNRAS, 74, 132
Rood, H. J. 1965, AJ, 70, 689
Ryś, A., Koleva, M., Falcón-Barroso, J., et al. 2015, MNRAS, 452, 1888
Saglia, R. P., Opitsch, M., Erwin, P., et al. 2016, ApJ, 818, 47
Saha, K., Martinez-Valpuesta, I., & Gerhard, O. 2012, MNRAS, 421, 333
Sahu, N., Graham, A. W., Davis, B. L., 2019, ApJS, submitted
Saito, M. 1979, PASJ, 31, 181
Sancisi, R., Fraternali, F., Oosterloo, T., & van der Hulst, T. 2008, The Astronomy and Astrophysics Review, 15, 189
Sandage, A., & Binggeli, B. 1984, AJ, 89, 919
Sandage, A., Binggeli, B., & Tammann, G. A. 1985, AJ, 90, 1759
Sanders, R. H., & McGaugh, S. S. 2002, ARA&A, 40, 263
Savorgnan, G. A. D., & Graham, A. W. 2016, ApJS, 222, 10
Savorgnan, G. A. D., Graham, A. W., Marconi, A., & Sani, E. 2016, ApJ, 817, 21
Schaye, J., Crain, R. A., Bower, R. G., et al. 2015, MNRAS, 446, 521
Schlafly, E. F., & Finkbeiner, D. P. 2011, ApJ, 737, 103
Schombert, J. M. 1986, ApJS, 60, 603
Schulze, F., Remus, R.-S., Dolag, K., et al. 2018, MNRAS, 480, 4636
Schweizer, F. 1986, Science, 231, 227
Schweizer, F., & Seitzer, P. 1988, ApJ, 328, 88
Scott, N., Davies, R. L., Houghton, R. C. W., et al. 2014, MNRAS, 441, 274
Seigar, M. S., Graham, A. W., & Jerjen, H. 2007, MNRAS, 378, 1575
Sérsic, J.-L. 1963, Boletin de la Asociacion Argentina de Astronomia, 6, 41
Sérsic, J.L. 1968a, Atlas de galaxias australes
Sérsic, J. L. 1968b, Bulletin of the Astronomical Institutes of Czechoslovakia, 19, 105
Shapley, H. 1951, Publications of Michigan Observatory, 10, 79
Shen, S., Mo, H. J., White, S. D. M., et al. 2003, MNRAS, 343, 978
Somerville, R. S., & Davé, R. 2015, ARA&A, 53, 51
Somerville, R. S., Hopkins, P. F., Cox, T. J., Robertson, B. E., & Hernquist, L. 2008, MNRAS, 391, 481
Stark, D. V., Kannappan, S. J., Wei, L. H., et al. 2013, ApJ, 769, 82
Steinborn, L. K., Dolag, K., Hirschmann, M., Prieto, M. A., & Remus, R.-S. 2015, MNRAS, 448, 1504
Stewart, K. R., Bullock, J. S., Wechsler, R. H., & Maller, A. H. 2009, ApJ, 702, 307
Stewart, K. R., Bullock, J. S., Wechsler, R. H., Maller, A. H., & Zentner, A. R. 2008, ApJ, 683, 597
Stiavelli, M., Miller, B. W., Ferguson, H. C., et al. 2001, AJ, 121, 1385
Strom, S. E., & Strom, K. M. 1978, AJ, 83, 732 van Dokkum PG. 2010. Ap. J. 720:723–41
Taylor, P., Federrath, C., & Kobayashi, C. 2017, MNRAS, 469, 4249
Taylor, P., & Kobayashi, C. 2014, MNRAS, 442, 2751
Terzić, B., & Graham, A. W. 2005, MNRAS, 362, 197
Terzić, B., & Sprague, B. J. 2007, MNRAS, 377, 855
Thomas, J., Saglia, R. P., Bender, R., Erwin, P., & Fabricius, M. 2014, ApJ, 782, 39 al., 2007. ApJ, 671:285–302
Toloba, E., Guhathakurta, P., Boselli, A., et al. 2015, ApJ, 799, 172
Tolstoy, E., Hill, V., & Tosi, M. 2009, ARA&A, 47, 371
Toomre, A., & Toomre, J. 1972, ApJ, 178, 623
Tonry, J. L., Blakeslee, J. P., Ajhar, E. A., & Dressler, A. 1997, ApJ, 475, 399
Trayford, J. W., & Schaye, J. 2018, MNRAS, submitted, arXiv:1812.06984
Tremonti, C. A., Heckman, T. M., Kauffmann, G., et al. 2004, ApJ, 613, 898
Trujillo, I., Förster Schreiber, N. M., Rudnick, G., et al. 2006, ApJ, 650, 18 RS. 2007. MNRAS 382:109–20
Trujillo, I., Graham, A. W., & Caon, N. 2001, MNRAS, 326, 869
van den Bergh, S. 2008, A&A, 490, 97
van den Bosch, R. C. E. 2016, ApJ, 831, 134
van Dokkum, P. G., Franx, M., Kriek, M., Holden, B., Illingworth, G. D., et al. 2008, ApJL, 677, L5
Veilleux, S., Cecil, G., & Bland-Hawthorn, J. 2005, ARA&A, 43, 769
Vennik, J., Richter, G. M. 1994, Astron. Nachr., 315, H3, 245
Visvanathan, N., & Sandage, A. 1977, ApJ, 216, 214
Vogelsberger, M., Genel, S., Springel, V., et al. 2014, MNRAS, 444, 1518
Wang, Y., Vogelsberger, M., Xu, D., et al. 2019, MNRAS, submitted, arXiv:1811.06545
Wei, L. H., Kannappan, S. J., Vogel, S. N., & Baker, A. J. 2010, ApJ, 708, 841
Weinberger, R., Springel, V., Pakmor, R., et al. 2018, MNRAS, 479, 4056
Weinzirl, T., Jogee, S., Khochfar, S., Burkert, A., & Kormendy, J. 2009, ApJ, 696, 411
Wirth, A., & Gallagher, J. S., III 1984, ApJ, 282, 85
Wolf, J. 2011, in Astrophysical Dynamics: From Stars to Galaxies, IAU Symposium, ed. N. H. Brummell, A. S. Brun, M. S. Miesch, Y. Ponty (Vol. 271), 110
Wolf, J., Martinez, G. D., Bullock, J. S., et al. 2010, MNRAS, 406, 1220
Young, C. K., Currie, M. J. 1994, MNRAS, 268, L11
Young, C. K., Currie, M. J. 1995, MNRAS, 273, 1141
Zemp, M. 2014, ApJ, 792, 124
Zwicky, F., & Kowal, C. T. 1968, Catalogue of Galaxies and of Clusters of Galaxies, Volume VI. Pasadena, CA: California Institute of Technology
Zwicky, F., & Zwicky, M. A. 1971, Guemligen: Zwicky

https://doi.org/10.1017/pasa.2019.23 Published online by Cambridge University Press